TÉCNICO LISBOA

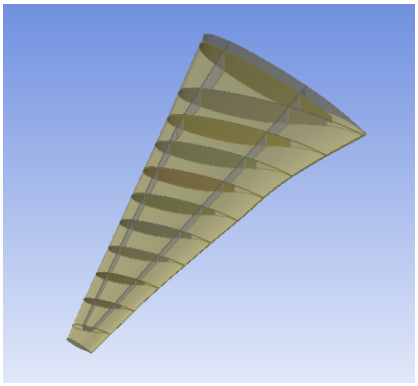

Model Order Reduction for Aircraft Structural Analysis

Bernardo Manuel Guerreiro Sequeira

Thesis to obtain the Master of Science Degree in

Aerospace Engineering

Supervisors: Prof. Fernando José Parracho Lau
Dr. Frederico José Prata Rente Reis Afonso

Examination Committee

Chairperson: Prof. Filipe Szolnoky Ramos Pinto Cunha
Supervisor: Prof. Fernando José Parracho Lau
Member of the Committee: Prof. Afzal Suleman

June 2019

I have the pleasure of having the most amazing people as a part of my life. I dedicate this thesis to all of them.

Acknowledgments

I would like to thank to my thesis supervisors, Prof. Fernando Lau and Prof. Frederico Afonso, who always showed full interest and availability in the work done for my thesis. Without their thorough help, it would be really difficult to finish this challenge. I would also like to thank to my faculty, Instituto Superior Técnico, for giving me the opportunity to study the subject, which has always been the main target of my curiosity. This opportunity has given me the chance of having a career related to aeronautics, which has always been a dream of mine since I was really young.

I also have to thank dearly to my family. They are the ones responsible for the foundations of my education. It was always their example and advices which inspired me the most.

Resumo

A ordem, ou dimensão, de modelos estruturais dinâmicos aplicados a estruturas aeroespaciais é bastante elevada. Consequentemente, o tempo de cálculo aplicado na sua solução pode tornar-se insustentável, em particular quando afeto à Otimização Multidisciplinar, como no caso da plataforma NOVEMOR. Esta tese apresenta o estudo da possibilidade de reduzir modelos correspondentes a estruturas aeroespaciais, diminuindo o tempo de cálculo e mantendo a precisão da solução. Primeiramente, conduziu-se uma pesquisa incidente nos métodos de redução de ordem com foco na aplicação a modelos estruturais, que demonstrou a predominância de métodos que usam o conceito de coordenadas generalizadas. As bases vetoriais que definem o espaço vetorial destas coordenadas são definidas por vetores de Ritz, vetores próprios de vibração livre ou vetores próprios ortogonais. Após a definição destas bases vetoriais, os modelos reduzidos podem ser formulados com o auxílio de determinadas técnicas como a Projeção de Galerkin e a Redução por Mínimos Quadrados. Posteriormente, foram selecionados modelos de referência aos quais foram aplicados os métodos identificados como mais adequados. Com o resultado desta aplicação, alcançou-se uma melhor compreensão destes métodos e procedeu-se a uma seleção adequada para o alcance do objetivo: reduzir um modelo estrutural referente a uma estrutura aeroespacial. Como exemplo prático foi formulado um modelo estrutural duma asa de avião comercial. Os métodos de redução aplicados a esse modelo envolvem as duas técnicas já mencionadas, usando vetores próprios ortogonais. A redução deste modelo resultou numa diminuição considerável do tempo necessário para a sua solução, mantendo, no entanto, a precisão da mesma.

Palavras-chave: Redução de Modelos, Projeção de Galerkin, Redução por Mínimos Quadrados, Cálculo Estrutural, Decomposição Própria Ortogonal, Método dos Elementos Finitos.

Abstract

The order, or dimension, of the structural dynamic models applied to airframe structures is considerably high. Consequently, the computation time involving these models can become unsustainable when it comes to MultiDisciplinary Optimization, like in the case of the NOVEMOR platform. This thesis studies the possibility of reducing the mentioned airframe models, thus resulting in a precise solution, but with less computational time spent in the solving process. Firstly, a research on the reduction methods was made, with focus on the ones which had applications to structural dynamics. This research revealed the prevalence of methods which used the concept of generalized coordinates. The vector basis which defines the vector space of these coordinates are formulated using Ritz vectors, free vibration eigenmodes or proper orthogonal modes. After defining this basis, the reduced models can be formulated using techniques like the Galerkin Projection or the Least Mean Square Reduction. After this research, some reference models were chosen and the most adequate reduction methods were applied to them. As a result of this implementation, a better understanding of the behaviour of these methods was obtained and an adequate selection of these reductions could be made in order to achieve the goal of this thesis: reducing an airframe structural model. A wing structure model from a commercial aircraft was formulated as a case study. The reduction methods applied in this model used the two techniques already mentioned above, exploiting the proper orthogonal modes. The reduction of this model resulted in a considerable decreasing of the computation time necessary for its solving process, maintaining, however, the precision of the solution.

Keywords: Model Order Reduction, Galerkin Projection, Least Mean Square Reduction, Structural Analysis, Proper Orthogonal Decomposition, Finite Element Method

Contents

List of Tables

List of Figures

Nomenclature

Greek symbols

α	Angle of attack.
ΔS	Snapshot spacing.
η	Modal Coordinates.
$\mathbf{\Sigma}$	Covariance Matrix.
μ	Air Dynamic Viscosity.
ω	Eigenfrequencies.
ω_c	Center frequency.
Φ	Eigenbasis.
ϕ	Eigenvalues.
Ψ	Reduction basis for CMS.
ψ	Augmentation basis.
ρ	Air density.

Roman symbols

$\mathbf{B}$	POD reduction basis.
b	Wingspan.
$\bar{c}$	Mean chord.
C_D	Coefficient of drag.
C_L	Coefficient of lift.
$\mathbf{E}$	Damping Matrix.
e_{colin}	Colinear error.
e_{ortho}	Orthogonal error.

e_{out} Output error.

$\mathbf{F}$ Force vector.

$\mathbf{G}$ Ritz spatial vector (loading pattern).

$\mathbf{H}(t)$ Time dependent vector associated with $\mathbf{G}$.

$\mathbf{K}$ Stiffness matrix.

$\mathbf{M}$ Mass matrix.

$\mathbf{p}$ CMS coordinates.

$\mathbf{Q}$ Snapshot Matrix.

$\mathbf{q}$ POD ROM coordinates.

$\mathbf{q}_m$ Ritz basis.

$\mathbf{q}_{HDM}$ HDM coordinates.

$\mathbf{q}_{ROM}$ ROM coordinates.

Re Reynolds Number.

S Wing Area.

$\mathbf{T}_G$ Global mapping matrix.

$\mathbf{t}_{HDM}$ HDM computational time duration.

$\mathbf{t}_{ROM}$ ROM computational time duration.

t_r Time Reduction.

U Flow Velocity.

$\mathbf{V}_m$ Ritz reduction basis.

$\mathbf{v}_n$ Ritz vector.

$\mathbf{X}$ Displacement Vector.

$y+$ Height of inflation zone.

Subscripts

b Boundary degree of freedom index.

e Excessive degree of freedom index.

i Interior degree of freedom index.

j Computational index.

m Master degree of freedom index.

r Rigid Body degree of freedom index.

s Slave degree of freedom index.

Superscripts

$\ddot{}$ Second derivative.

$\dot{}$ First derivative.

c Component index.

T Transpose.

Glossary

AI	Artificial Intelligence.
BEM	Boundary Element Method.
CFD	Computational Fluid Dynamics.
CMS	Component Mode Synthesis.
CPU	Computer Processor Unit.
DS	Dynamic Substructuring.
FEM	Finite Element Method
HDM	High Definition Model.
LDRV	Load Dependent Ritz Vectors.
LMSQ	Least Mean Square.
MDO	Multi-Disciplinar Optimization.
MEMS	Micro Electro-Mechanical System.
ODE	Ordinary Differential Equation.
PCA	Principal Component Analysis.
POD	Proper Orthogonal Decomposition.
POM	Proper Orthogonal Mode.
POV	Proper Orthogonal Value.
RAM	Random Access Memory.
ROM	Reduced Order Model.
SVD	Singular Value Decomposition

Chapter 1

Introduction

1.1 Motivation

This thesis is made within the scope of the NOVEMOR project's Multidisciplinary Design Optimization (MDO) framework that has been developed at IST for aircraft conceptual design[1]. In order to have a better Optimization Framework, one of the key objectives is to have not too costly computations, so that a frequent model computation could be obtained without a large cost on simulation time, thereby easing the optimization process. To reach that goal in this framework, the aircraft structure, at a conceptual design phase, is modeled via beams and discretized by the finite element method (FEM). Nonetheless these structural simplifications of the high definition structural model are not the most accurate, since they neglect some of the physical and geometric properties of the model. In what concerns aerodynamics, despite the possibility of the utilization of a surrogate model applied to derivation of the aerodynamic forces of the entire aircraft, it still neglects the physical sense of the problem, because surrogate models are limited to fit a parametric function that best describes the behaviour of a certain sample of data, thus not bearing in mind the physical model of the system.[2]

Therefore the ideal solution would be a model that could keep the ”physics” of the problem and at the same time reduce the order of the high fidelity model or high definition model (HDM). Since the mentioned framework has already explored the physical idealization and the surrogate model technique, there is one method left to be explored, which is called Model Order Reduction (MOR). This technique considers the partial differential equations or ordinary differential equations (ODEs) of the HDM and derives a much smaller model (less degrees of freedom) called reduced order model (ROM). Consequently this new model is supposed to take less time to reproduce the response of the system and the fact that it takes the model differential equations into consideration, will imply that the physics of the model are not neglected, hence improving the accuracy of the results when compared to the ones provided by the neglected models or idealized structural models.

There are some techniques which incorporate both surrogate and MOR methods. These techniques are usually applied to black-box modelling or parametric analysis. They will use interpolation methods to find the ROM that best fits a certain sample of the problem data, this data consists in ROMs that

were previously derived with different parameters, so that a kind of manifold interpolation is made using these ROMs[3–6]. Recently there has also been some research in the use of artificial intelligence (AI) methods in the field of computational mechanics, it has been proven that AI offers advantages to deal with problems associated with uncertainties and is an effective aid to solve such complex models [7]. These techniques can also be able to make the process of decision making faster, decrease error rates and increase computational efficiency [7]. One of the AI methods used in computational mechanics is deep learning, by using this method a new way of numerical quadrature for the FEM stiffness matrices has been developed, in which a specific optimized quadrature rule superior in accuracy to the standard Gauss-Legendre quadrature is obtained [8]. Since this kind of methods are still in a early stage of development, this thesis will focus only on the MOR techniques.

1.2 Topic Overview

On typical structural engineering projects, HDMs are required. To perform a dynamic analysis on these models, numerical methods are needed, such as the FEM or the boundary element method (BEM). In these methods the models need to be represented with a high number of degrees of freedom, thus increasing the complexity of the analysis. Due to this intricacy, the solving times for these methods will be unsustainable, since structural dynamic analyses require parametric studies of the system responses under a load or any phenomena that can change over time, for example, civil structures under seismic loads, changes of loads in a structure, machinery, structural health monitoring to predict the variation of the dynamic behavior after damages such as delaminations or impacts, a crack onset or growth, or even a blade loss event in an aircraft [9]. Hence becoming really expensive when performed over large and complex structures, because they take important computer resources (CPU time, RAM memory and disk space) and can even block the expensive licenses of professional finite element software [9]. Therefore, MOR techniques can be of the most importance, since simulation times can drastically decrease while maintaining the precision comparing to the HDM direct solving, but still requiring some RAM memory, so that the algebraic operations needed in their algorithms can be successfully made.

This kind of solution is of many interest for the aerospace/aeronautical industry, since its product design requires a lot of simulation time, because in all the disciplines of an aeronautical project (aerodynamics, structures, materials, among others) the main goal is to optimize the product components, that usually are based on HDMs. Reducing this computation time would increase not only the efficiency of the design of each aircraft component, but also the efficiency of the full design of the aircraft in question.

1.3 Objectives

The main goal for this thesis is to explore the main MOR techniques, which can be of interest for the structural analysis of aircraft structures. So to reach this goal, the following objectives are of importance for the thesis:

- Search for MOR methods applied in engineering problems and their latest scientific developments.
- Implementation of these techniques to structural models.
- Comparing the results of each technique on each structural model (benchamrk problems), with the purpose of establishing their pros and cons.
- Application of MOR to a structural model of an aircraft component.

Thus the structural analysis of several models will be presented, with focus on dynamic structural analysis, since the effects of the model reduction (decrease in simulation time) will be more noticed in this case comparing to the static analysis reduction.

1.4 Thesis Outline

To follow the respective objectives, the thesis will be structured by the subsequent chapters:

- MOR methods
- Benchmark of reduced models
- Application of MOR methods to a structural dynamic problem of an aircraft component
- Conclusion

The first chapter will present the methods found during the research on MOR techniques, with emphasis on the ones used on structural dynamics. The second chapter will discuss the implementation of these techniques on structural models, with the purpose of comparing the simulation time obtained using the HDM and the reduced models, thus establishing several MOR benchmarks. The third chapter will explore the development of a structural model of an aircraft structure and the application of the most adequate MOR methods to reduce the simulation time in the respective model. Conclusions will be stated on the last chapter.

Chapter 2

Model Order Reduction Methods

In this chapter the MOR methods found in the research for the state of the art of this subject will be covered. The focus of this research was done for the reduction methods with more relevance in the structural dynamics field of study. Each method will have its theoretical fundamentals and mathematical formulation described, so that its implementation can be easily applied in chapter 3.

If one wants to categorize the MOR methods, considering the type of variables employed in the reduced model, three types of reduction can be obtained, the ones using: physical coordinates; generalized coordinates; and hybrid coordinates. For this reason, the following chapter will be divided in the three categories mentioned here.

The generalized coordinate methods require the computation of certain eigenproblems and generally they are developed through a coordinate transformation matrix, which makes the connection between the physical coordinates space of the structural HDM and the retained coordinates of the ROM [9]. This transformation matrix is called the reduced basis. The connection between the HDM space and the reduce one is usually made via orthogonal projections, which are commonly referred to as Galerkin projections [10], but there are also other alternatives to the Galerkin Projections, which are going to be mentioned in the section 2.3 of this thesis. The hybrid coordinates are a mix of these two types of coordinates.

Another issue involving all the MOR techniques is the assumption of non-linearities in a certain model. This issue will not be addressed in this thesis, but it can be found in several references, such as [11–13].

2.1 Physical Coordinates

The MOR method that keeps the physical coordinates of the HDM in the reduced model is called the condensation method. This technique is based on the removal of undesirable degrees of freedom of the HDM and was firstly used in static problems, but several dynamic analyses use this technique under certain assumptions.

So as it was to be expected the formulation of this method begins with the static equations of equi-

librium:

$$\mathbf{KX} = \mathbf{F}, \tag{2.1}$$

where $\mathbf{K}$ is the stiffness matrix, $\mathbf{X}$ the displacement vector containing the displacements of each degree of freedom and $\mathbf{F}$ the force vector. The key of the condensation method is based on dividing the degrees of freedom of the HDM in to two types: the master degrees of freedom (the retained ones) and the slave degrees of freedom (the deleted ones). With this assumption the equilibrium equation can be represented as:

$$\begin{bmatrix} \mathbf{K}_{mm} & \mathbf{K}_{ms} \\ \mathbf{K}_{sm} & \mathbf{K}_{ss} \end{bmatrix} \begin{Bmatrix} \mathbf{X}_m \\ \mathbf{X}_s \end{Bmatrix} = \begin{Bmatrix} \mathbf{F}_m \\ \mathbf{F}_s \end{Bmatrix} \tag{2.2}$$

$\mathbf{X}_s$ is the displacement vector of the slave degrees of freedom, $\mathbf{X}_m$ the displacement vector of the master degrees of freedom and the indices m and s correspond to master and slave, respectively. Expanding equation 2.2 in to two equations, namely,

$$\mathbf{K}_{mm}\mathbf{X}_m + \mathbf{K}_{ms}\mathbf{X}_s = \mathbf{F}_m \tag{2.3}$$

$$\mathbf{K}_{sm}\mathbf{X}_m + \mathbf{K}_{ss}\mathbf{X}_s = \mathbf{F}_s, \tag{2.4}$$

expressing 2.4 in terms of $\mathbf{X}_m$, the following equation is obtained

$$\mathbf{X}_s = -\mathbf{K}_{ss}^{-1}\mathbf{K}_{sm}\mathbf{X}_m + \mathbf{K}_{ss}^{-1}\mathbf{F}_s, \tag{2.5}$$

introducing 2.5 into 2.3 yields

$$\mathbf{K}_R\mathbf{X}_m = \mathbf{F}_R, \tag{2.6}$$

$\mathbf{K}_R$ and $\mathbf{F}_R$ are the reduced stiffness matrix and equivalent force vector, respectively. Both corresponding to the masters. The algebraic manipulation to form $\mathbf{K}_R$ and $\mathbf{F}_R$ is the

$$\mathbf{K}_R = \mathbf{K}_{mm} - \mathbf{K}_{ms}\mathbf{K}_{ss}^{-1}\mathbf{K}_{sm} \tag{2.7}$$

$$\mathbf{F}_R = \mathbf{F}_m - \mathbf{K}_{ms}\mathbf{K}_{ss}^{-1}\mathbf{F}_s \tag{2.8}$$

Assuming that $\mathbf{F}_s = 0$, with the only purpose of deriving the relation between the displacement vector of the masters and the displacement vector of the slaves, trough 2.5, thus leading to

$$\mathbf{X}_s = \mathbf{R}_G\mathbf{X}_m \tag{2.9}$$

So the condensation matrix is represented by $\mathbf{R}_G$ and is define by

$$\mathbf{R}_G = -\mathbf{K}_{ss}^{-1}\mathbf{K}_{sm} \tag{2.10}$$

This condensation method was first proposed in [14] and is called the Guyan condensation. Due

to the omission of the dynamic effects, this method can also be called static condensation, but for the contrary, as it will be shown next, this method can be applied dynamic problems too. Nevertheless, another definition should be presented

$$\mathbf{X} = \begin{Bmatrix} \mathbf{X}_m \\ \mathbf{X}_s \end{Bmatrix} = \mathbf{T}_G \mathbf{X}_m \tag{2.11}$$

$\mathbf{T}_G$ is the global mapping matrix and it basically relates the responses at all degrees of freedom to those at the masters. It can also be defined as

$$\mathbf{T}_G = \begin{bmatrix} \mathbf{I} \\ \mathbf{R}_G \end{bmatrix}, \tag{2.12}$$

in which $\mathbf{I}$ is the identity matrix. Using equation 2.11 into 2.1 and premultiplying both sides by the transpose of $\mathbf{T}_G$ results in

$$\mathbf{K}_G \mathbf{X}_m = \mathbf{F}_G, \tag{2.13}$$

where $\mathbf{K}_G$ and $\mathbf{F}_G$ are the reduced stiffness matrix and reduced force vector, respectively. They can be represented as

$$\mathbf{K}_G = \mathbf{T}_G^T \mathbf{K} \mathbf{T}_G, \quad \mathbf{F}_G = \mathbf{T}_G^T \mathbf{F} \tag{2.14}$$

Now considering the dynamic equation of equilibrium of a full model without damping

$$\mathbf{M}\ddot{\mathbf{X}}(t) + \mathbf{K}\mathbf{X}(t) = \mathbf{F}(t) \tag{2.15}$$

$$\begin{bmatrix} \mathbf{M}_{mm} & \mathbf{M}_{ms} \\ \mathbf{M}_{sm} & \mathbf{M}_{ss} \end{bmatrix} \begin{Bmatrix} \ddot{\mathbf{X}}_m(t) \\ \ddot{\mathbf{X}}_s(t) \end{Bmatrix} + \begin{bmatrix} \mathbf{K}_{mm} & \mathbf{K}_{ms} \\ \mathbf{K}_{sm} & \mathbf{K}_{ss} \end{bmatrix} \begin{Bmatrix} \mathbf{X}_m(t) \\ \mathbf{X}_s(t) \end{Bmatrix} = \begin{Bmatrix} \mathbf{F}_m(t) \\ \mathbf{F}_s(t) \end{Bmatrix} \tag{2.16}$$

As it was said before, the same assumptions that were made before in this section (static analysis) have to be made in the dynamic analysis too, in order to use the Guysian method. This includes ignoring the inertial effects ($\ddot{\mathbf{X}}_m(t) = 0$ and $\ddot{\mathbf{X}}_s(t) = 0$) and considering $\mathbf{F}_s(t) = 0$ for the same purpose as the example before, that is, only to obtain the relation between the degrees of freedom of the masters and the slaves, thus obtaining the same relation as 2.11. The difference in the case of the dynamic analysis is that the equation 2.11 will be differentiated in both sides and since the coordinate transformation matrix $\mathbf{T}_G$ is not time dependent, the following expression can be obtained

$$\ddot{\mathbf{X}}(t) = \mathbf{T}_G \ddot{\mathbf{X}}_m(t) \tag{2.17}$$

So, analogously to the static problem, the reduced mass matrix can be represented as

$$\mathbf{M}_G = \mathbf{T}_G^T \mathbf{M} \mathbf{T}_G = \mathbf{M}_{mm} + \mathbf{K}_{ms}\mathbf{K}_{ss}^{-1}\mathbf{M}_{ss}\mathbf{K}_{ss}^{-1}\mathbf{K}_{sm} - \mathbf{K}_{ms}\mathbf{K}_{ss}^{-1}\mathbf{M}_{sm} - \mathbf{M}_{ms}\mathbf{K}_{ss}^{-1}\mathbf{K}_{sm}, \tag{2.18}$$

thus obtaining the reduced model described by

$$\mathbf{M}_G\ddot{\mathbf{X}}_m(t) + \mathbf{K}_G\mathbf{X}_m(t) = \mathbf{F}_G(t), \tag{2.19}$$

where $\mathbf{K}_G$ and $\mathbf{F}_G$ are equal to the ones derived in the static case. Although the inertial effects were neglected in the beginning of the formulation of the ROM, it can be seen that they are taken into account when the reduced mass matrix is introduced in the model.

From the previous formulations it can be noticed that the laborious calculation of the matrix $\mathbf{K}_{ss}^{-1}$ is needed for the derivation of the condensation matrix. To alleviate the computational complexity of this inverse procedure, one can use the Gauss-Jordan elimination, as it is applied in [15].

It has to be highlighted that the main assumption made in this method is that for lower frequency modes, inertial forces on slaves are less relevant than the elastic forces transmitted by the masters, thus the mass of the structure is distributed among only the master degrees of freedom [16]. Therefore this method has an error in the solution due to this approximation of the inertial terms. The error can be measured by the relative error in each eigenvalue i (ε_i) and by the error of the mode shape γ_i, these errors can be defined as:

$$\varepsilon = \frac{\lambda_{r,i} - \lambda_i}{\lambda_{r,i}} \tag{2.20}$$

$$\gamma_i = 1 - \left| \frac{\mathbf{D}_{r,i}^T \mathbf{D}_i}{|\mathbf{D}_{r,i}^T||\mathbf{D}_i|} \right| \tag{2.21}$$

The information needed to derive this errors is given by $(\mathbf{K}_r - \lambda_r\mathbf{M}_r)\mathbf{D}_r = \mathbf{0}$ and $(\mathbf{K} - \lambda\mathbf{M})\mathbf{D} = \mathbf{0}$. Regarding the choice of master and slave degrees of freedom, the relation $\frac{k_{ii}}{m_{ii}}$ can establish a good option for this issue, according to Matta's scheme, the higher the values of $\frac{k_{ii}}{m_{ii}}$ of the slaves, the lower the error introduced during the condensation [17].

There are many other approaches on dynamical analysis using condensation as a MOR technique, like dynamic condensation, iterative methods for dynamical condensation, dynamic condensation of nonclassically damped models. [14][18]

2.2 Projection Based Generalized Coordinates

The main methods that use generalized coordinates with Galerkin projections are: the modal coordinates methods, Ritz vector methods, Component Modal Synthesis (CMS) and Proper Orthogonal Decomposition (POD). The common approach of all these methods is the use of a reduction basis matrix that establishes the relation between the physical coordinate space and the generalized coordinate space.

Since the mejority of these method is built *a posteriori*, that is, the methods is only developed with already derived results of the HDM, one may wonder about the sense of applying these techniques, but actually there are two approaches for this question [19]:

- Solving the HDM in a small time interval, hence allowing the extraction of the basis that defines the reduced model. Such model is then used to derive the results for the remaining time interval;
- Solving the HDM in the entire time interval, then use the corresponding reduced model to solve identical problems (small parametric changes);

This section will have 5 parts, one for each mentioned MOR technique.

2.2.1 Modal Coordinates Methods

The modal coordinates methods can be seen as a combination of the standard superposition method and the modal truncation methods. The standard superposition method reduces a large scale finite element model by approximating the physical coordinates of the HDM into the modal space, by using the eigenvector matrix of the system as its reduction basis, or in this case, the eigenbasis. The modal truncation method is based on ignoring the modes that are of no use for a certain analysis. Since few modes have a significative importance for a certain response, usually the modal coordinate space will be much smaller (lower dimension) than the physical coordinate space. Figure 2.1 represents a schematic of this method.

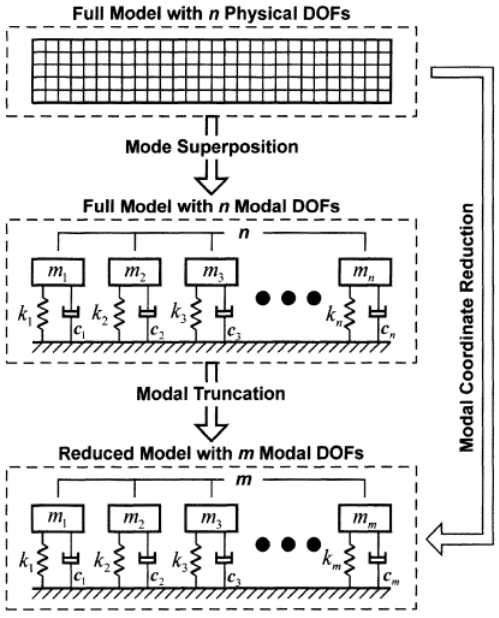

Figure 2.1: Schematic of Modal Coordinate reduction [20]

There are some interesting points about this technique that need to be mentioned, such as [20]:

- The used mode shape vectores do not span the complete space;
- The computation of eigenvectors for large systems is very expensive and time consuming;
- The number of eigenmodes required for satisfactory accuracy is difficult to estimate *a priori*, which limits the automatic selection of eigenmodes;

- The eigenbasis ignores important information related to the specific loading characteristics, such that the computed eigenvectors can be nearly orthogonal to the applied loading and consequently do not participate in the solution;

There are three main variants of this method: mode displacement method, mode acceleration method and modal truncation augmentation method. The latter two techniques are improvements of the first one.

In the next sections the mode displacement method and its variants will be treated in detail.

Mode Displacement Method

Recalling the dynamic equilibrium equations (neglecting damping) from the last method (2.15),

$$\mathbf{M}\ddot{\mathbf{X}} + \mathbf{K}\mathbf{X} = \mathbf{F} \tag{2.22}$$

.

This method is based on the free vibration modes of the system, thus an imperative assumption is considering $\mathbf{F} = \mathbf{0}$, for the mode calculation. This assumption leads to the following eigenvalue problem

$$(\mathbf{K} + \omega_j^2 \mathbf{M})\phi_j = \mathbf{0}, \tag{2.23}$$

in which ϕ_j is the mode shape vector (eigenvectors) corresponding to the eigenfrequency ω_j, with $j \in [1, ..., N]$, where N is the size of the HDM. Taking into consideration the expansion procedure and the derived eigenvectors, one can represent the displacement vector as

$$\mathbf{X} = \sum_{j=1}^{N} \phi_j \eta_j, \tag{2.24}$$

where η_j is a set of modal coordinates. The objective of using the expansion procedure is to keep just some relevant eigenvectors that will correspond to a certain eigenfrequency, commonly the lowest frequencies, since the major part of structures operate at those frequencies. The number of modes kept will be equal to the order of the ROM. With this mode selection a truncation is obtained

$$\mathbf{X} = \sum_{j=1}^{K} \phi_j \eta_j + \sum_{j_t=K-1}^{N} \phi_{j_t} \eta_{j_t}, \tag{2.25}$$

considering that j and j_t are the selected and truncated mode indices, respectively. The last displacement vector formulation (2.25) can also be represented in:

$$\mathbf{X} = \mathbf{\Phi}\eta, \quad \mathbf{\Phi} = \begin{bmatrix} \phi_1 \ \phi_2 \ \phi_2 ... \phi_K \end{bmatrix} \tag{2.26}$$

So the formulation of the reduced model can be represented as

$$\mathbf{M}_r \ddot{\eta} + \mathbf{K}_r \eta = \mathbf{f}_r, \tag{2.27}$$

where

$$\mathbf{M}_r = \mathbf{\Phi}^T \mathbf{M} \mathbf{\Phi}, \quad \mathbf{K}_r = \mathbf{\Phi}^T \mathbf{K} \mathbf{\Phi}, \quad \mathbf{f}_r = \mathbf{\Phi}^T \mathbf{f} \tag{2.28}$$

This representation just demonstrates the Galerkin projection of the original equations of motion into the generalized coordinate space, thus using the eigenbasis $\mathbf{\Phi}$. There are two important properties of the modes in general, that need to be mentioned:

- The orthogonality of the mode with respect to the excitation $\phi_j^T \mathbf{f}$;
- The closeness of the eigenfrequency of the mode with respect to the excitation spectrum of interest;

Mode Acceleration Method

This variant is based on a static correction method, it accounts for the static contribution of the truncated modes. Adding this contribution will increase the accuracy of the reduced model, since the truncated modes have a significant static contribution on the response for low frequencies. This contribution can be formulated as follows

$$\mathbf{X} = \mathbf{\Phi} \eta + \mathbf{X}_{cor}. \tag{2.29}$$

To obtain the static correction term $\mathbf{X}_{cor}$, the truncated formulation for the acceleration is replaced in equation 2.15, after some algebraic manipulation the correction can be obtained with

$$\mathbf{X}_{cor} = \Big(\mathbf{K}^{-1} - \sum_{j=1}^{K} \frac{\phi_j \phi_j^T}{\omega_j^2} \Big) \mathbf{f}. \tag{2.30}$$

Modal Truncation Augmentation Method

This method is just an extension of the mode acceleration method, the main addition to it is the use of the static correction as an additional direction for the truncation expansion, this can be showed by the next equation

$$\mathbf{X} = \sum_{j=1}^{K} \phi_j \eta_j + \mathbf{X}_{cor} \xi, \tag{2.31}$$

in which $\mathbf{X}_{cor}$ is given by equation 2.30 and ξ is an additional coordinate in the reduced system, the correction vector is included in the reduction basis, thus obtaining the following basis

$$\mathbf{\Psi} = \begin{bmatrix} \mathbf{\Phi} & \mathbf{X}_{cor} \end{bmatrix} \tag{2.32}$$

2.2.2 Ritz Vector Method

The Ritz vector method has been used for a long time in the reduction of large scale models [18] and it is a good alternative for the superposition methods, particularly when the structure is subjected to fixed

spatial distribution of dynamical loads and the eigenvectors basis is not the most adequate. This can happen occasionally when the eigenvectors, which are orthogonal to the loading, are not excited, even when their frequencies are in the loading frequency bandwidth [20]. Plus, applying the Ritz vectors in some eigenvalue problems has proven to be beneficial, particularly concerning the time performance of the numerical methods used in those problems [21].

A distinctive particular Ritz vector class referred as load-dependent Ritz vectors (LDRVs) is of particular interest. In this class of vectors loading information is used to generate them, consequently these vectors will automatically include static correction and their generation is usually less expensive than the computation of eigenvectors, mainly because few Ritz vectors are typically needed to achieve the same level of accuracy for a specific load. This dependence on the load distribution means every time the load is changed, the computation of the Ritz vectors has to be done again; this fact can be very time consuming.

The LDRV method has, as the first Ritz vector, the static deformation of a structure due to a particular applied load pattern; additional orthogonal vectors can be computed using inverse iteration and Gram-Schmidt orthogonalization presented later.

As always, the formulation of this method begins with the dynamic equation of equilibrium, but in this case the following has to be considered

$$\mathbf{F}(t) = \mathbf{G}\mathbf{H}(t) = \sum_{i=1}^{k} \mathbf{g} h_i(t), \tag{2.33}$$

thus introducing the following dynamic equation of equilibrium

$$\mathbf{M}\ddot{\mathbf{X}}(t) + \mathbf{K}\mathbf{X}(t) = \mathbf{F}(t) = \mathbf{G}\mathbf{H}(t), \tag{2.34}$$

where the spatial matrix $\mathbf{G}$ (loading patterns) and the time-dependent vector $\mathbf{H}(t)$ can be represented as

$$\mathbf{G} = \begin{bmatrix} \mathbf{g}_1 \ \mathbf{g}_2 \cdots \mathbf{g}_k \end{bmatrix} \qquad \mathbf{H}(t) = \begin{Bmatrix} h_1(t) \ h_2(t) \cdots h_k(t) \end{Bmatrix}^T \tag{2.35}$$

The relation between the physical coordinates $\mathbf{X}(t)$ and the generalized coordinates $\mathbf{q}_m(t)$ referred to as Ritz coordinates can be expressed as

$$\mathbf{X}(t) = \mathbf{V}_m \mathbf{q}_m(t), \tag{2.36}$$

in which $\mathbf{V}_m$ is the basis for the reduced space defined by the Ritz vectors. Such matrix can be represented as

$$\mathbf{V}_m = \begin{Bmatrix} \mathbf{v}_1 \ \mathbf{v}_2 ... \mathbf{v}_m \end{Bmatrix}, \tag{2.37}$$

where $\mathbf{v}_m$ are the derived Ritz vectors and m is equal to the order of the ROM. The projection into the

reduced basis and the respective reduced model can be obtained by the following equation

$$\mathbf{M}_r\ddot{\mathbf{q}}_m(t) + \mathbf{K}_r\mathbf{q}_m(t) = \mathbf{F}_r(t) = \mathbf{G}_r\mathbf{H}(t), \tag{2.38}$$

and the reduced matrices are presented below

$$\mathbf{M}_r = \mathbf{V}_m^T\mathbf{M}\mathbf{V}_m, \quad \mathbf{K}_r = \mathbf{V}_m^T\mathbf{K}\mathbf{V}_m, \quad \mathbf{F}_r = \mathbf{V}_m^T\mathbf{F}, \quad \mathbf{G}_r = \mathbf{V}_m^T\mathbf{G} \tag{2.39}$$

In the following sections, only a single load will be considered, thus $\mathbf{G}$ is a vector and $\mathbf{H}(t)$ a time-dependent vector

Static Ritz vector methods

In [22] this method is formulated using a special Krylov sequence. It begins by using the solution of the static equilibrium equation for a given load pattern, represented by

$$\hat{\mathbf{v}}_1 = \mathbf{K}^{-1}\mathbf{g} \tag{2.40}$$

this vector can be mass normalized as follows

$$\mathbf{v}_1 = \frac{\hat{\mathbf{v_1}}}{(\hat{\mathbf{v}}_1^T\mathbf{M}\hat{\mathbf{v}}_1)^{\frac{1}{2}}} \tag{2.41}$$

It is trivial to notice that the inertial term is neglected in the first step, but it is included in the successive steps to generate the new Ritz vectors

$$\tilde{\mathbf{v}}_\mathbf{i} = \mathbf{K}^{-1}\mathbf{M}\mathbf{v}_{i-1} \quad (i = 2, 3, ..., m) \tag{2.42}$$

Then the Gram-Schmidt mass orthogonalization and normalization are used for this vectors

$$M - Orthogonalization: \qquad \hat{\mathbf{v}}_i = \tilde{\mathbf{v}}_i - \sum_{j=1}^{i-1}(\mathbf{v}_j^T\mathbf{M}\tilde{\mathbf{v}}_i)\mathbf{v}_j \tag{2.43}$$

$$M - Normalization: \qquad \mathbf{v}_i = \frac{\hat{\mathbf{v}}_i}{\left(\hat{\mathbf{v}}_i^T\mathbf{M}\hat{\mathbf{v}}_\mathbf{i}\right)^{\frac{1}{2}}} \tag{2.44}$$

In each iteration one new Ritz vector is derived, thus the process continues until enough vectors are calculated, or no more independent vectors can be derived, or even if some stopping criteria is imposed. One of the stop criteria can be the participation factor $p_i = \mathbf{v}_i^T\mathbf{g}$ and it can be calculated for each one of the Ritz vectors.

Quasistatic Ritz Vector Methods

This method is an extension for the method explained in the last section. It employs a quasistatic procedure by letting the Ritz vectors span the configuration space at a desired frequency or frequencies.

The first quasistatic Ritz vector will be determined as

$$\hat{\mathbf{v}}_1 = (\mathbf{K} - \omega_\mathbf{c}^\mathbf{2}\mathbf{M})^{-1}\mathbf{g} \tag{2.45}$$

in which ω_c is denominated as the center frequency, since the frequency chosen is usually in the center of the spectrum that is being analyzed. Thus normalizing the respective Ritz vector one can obtain

$$\mathbf{v}_1 = \frac{\hat{\mathbf{v}}_1}{\left(\hat{\mathbf{v}}_1^T\mathbf{M}\hat{\mathbf{v}}_1\right)^{\frac{1}{2}}} \tag{2.46}$$

The next Ritz vectors ($i = 2, 3, ..., m$) can be calculated as follows

$$\tilde{\mathbf{v}}_i = (\mathbf{K} - \omega_c\mathbf{M})^{-1}\mathbf{M}\mathbf{v}_{i-1} \tag{2.47}$$

$$\hat{\mathbf{v}}_\mathbf{i} = \tilde{\mathbf{v}}_\mathbf{i} - \sum_{j=1}^{i-1}(\mathbf{v}_j^T\mathbf{M}\tilde{\mathbf{v}}_i)\mathbf{v}_j \tag{2.48}$$

$$\mathbf{v}_i = \frac{\hat{\mathbf{v}}_i}{\left(\hat{\mathbf{v}}_i^T\mathbf{M}\hat{\mathbf{v}}_\mathbf{i}\right)^{\frac{1}{2}}} \tag{2.49}$$

The physical meaning of the first Ritz vector is the representation of a normalized frequency response deformation mode, at the centering frequency ω_c, therefore the inertial term neglected in the static solution 2.40 is included in this method. If the ω_c is the only frequency defining the load, then $\mathbf{v}_1$ should describe the exact steady state deformation mode of the structure. That is why the choice of ω_c is fulcral, because if it is a major frequency in the analyzed frequency spectrum, then $\mathbf{v}_1$ gives the most likely deformation shape corresponding to that frequency. The Ritz vector $\tilde{\mathbf{v}}_\mathbf{2}$ will represent the frequency response deformation mode shape due to the inertial force $\mathbf{M}\mathbf{v}_1$, and so on. After mass orthonormalization, the next set of Ritz vectors will create a basis that will span a wider configuration space for the dynamic response.

There is also a participation factor for this method given by [21]

$$p_i = \frac{\mathbf{v}_i^T\mathbf{s}}{\sqrt{(\mathbf{v}_i^T\mathbf{v}_i)(\mathbf{s}^T\mathbf{s})}} \tag{2.50}$$

where

$$\mathbf{s} = (\mathbf{K} - \tilde{\omega}^2\mathbf{M})^{-1}\mathbf{g} \tag{2.51}$$

and it can be defined as the frequency response due to the loading pattern $\mathbf{g}$, while $\tilde{\omega}$ is a specified frequency. The maximum value of this parameter is 1 and it is verified when the Ritz vector exactly matches the frequency response deformation shape. For the choice of $\tilde{\omega}$, it has to be taken into account that this frequency should represent a dominant frequency of the loading pattern.

2.2.3 Component Mode Synthesis

This method will be introduced in the framework for dynamic substructuring (DS). The concept of DS is of major importance in the structural dynamic analysis of large scale systems, since its approach is focused on a componentwise analysis instead of a global analysis of the system. The principal advantages of this approach are [23]:

- The capability of analyzing large systems that cannot be evaluated as a whole, for example, a numerical model which the number of degrees of freedom is too big to solve in a reasonable time;
- Allowing an easier analysis of the local behaviour of the system, thus eliminating local subsystem behaviour which has no significant impact on the global system;
- Combining modeled parts (discritized or analytical) and experimentally identifying components;
- Sharing, combining and parallel processing of substructures from different project groups;

Considering a finite element model, one of its characteristics is the discretization of the domain in small finite elements that can be denominated as subdomains. These subdomains can be treated as ”first level” domain decomposition technique as represented in figure 2.2.3. The ”second level” decomposition is based on the discretization of the whole structure into substructures, which can be computed using parallel processing.

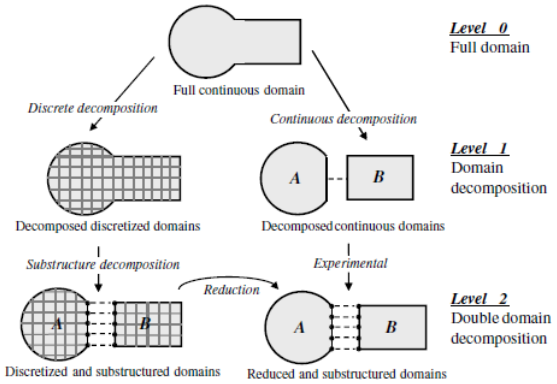

Figure 2.2: Dynamic substructuring and its relation to domain decomposition [23]

After the domain is discretized and substructured, the CMS enters in action by reducing the order of the substructured models. Then after finding an approximate solution in the subspace of the physical domain, the substructures need to be coupled. This is represented in by the ”reduction” arrow.

This DS technique can be used in three types of domain: physical, frequency and modal domain. Therefore the coupling process will have three variants: coupling in the physical, frequency or in the reduced component domain. This section will focus only on the last variant of coupling, since it is the situation of interest for the demonstration of the CMS. Another two points that need to be taken into account, when two substructures are to be coupled, are referenced below [23]:

- Compatibility condition: the displacements at the interface of each substructure need to be compatible.

- Equilibrium condition: the force equilibrium on the substructure's interface needs to be verified.

The formulation of these two fundamental conditions are respectively represented below

$$\mathbf{X}_b^{\alpha} = \mathbf{X}_b^{\beta}, \quad \hat{\mathbf{f}}_b^{\alpha} + \hat{\mathbf{f}}_b^{\beta} = 0 \tag{2.52}$$

The indices α and β correspond to the two hypothetical components of the whole system and the subscript b corresponds to the boundary elements of the components. The equilibrium equations represent the mutually reactive internal interface forces, which does not include the external forces applied at the interface.

Focusing now on the CMS method, there are three fundamental steps in this method: (1) division of a structure into components (substructuring); (2) definition of sets of component modes and; (3) coupling of the component mode models to form a reduced order model. The first step has already been considered along with the DS concept, so as a result of the substructuring the following dynamic equilibrium equation will be obtained:

$$\mathbf{M}^c\ddot{\mathbf{X}}^c(t) + \mathbf{K}^c\mathbf{X}^c(t) = \mathbf{f}^c(t) \tag{2.53}$$

where the superscript c refers to the componentwise elements, therefore the matrices and vectors $\mathbf{M}^c$, $\mathbf{K}^c$, $\mathbf{f}^c$ and $\mathbf{u}^c$ are the component mass matrix, stiffness matrix, force vector and displacement vector, respectively. As it is common in all the MOR techiniques that use generalized coordinates, the relation between the full order space and the reduced one is given by the Galerkin Projection scheme:

$$\mathbf{X}^c = \mathbf{\Psi}^c\mathbf{p}^c \tag{2.54}$$

in which the reduction matrix $\mathbf{\Psi}^c$ has the component modes as its columns. The component modes can have the following types: rigid-body modes; free vibration normal modes (eigenvectors); constraint modes; and attachment modes. With this being said the ROM can be represented as

$$\bar{\mathbf{M}}^c\ddot{\mathbf{p}}^c(t) + \bar{\mathbf{K}}^c\mathbf{p}^c(t) = \bar{\mathbf{f}}^c(t) \tag{2.55}$$

where

$$\bar{\mathbf{M}}^c = \mathbf{\Psi}^{cT}\mathbf{M}^c\mathbf{\Psi}^c, \quad \bar{\mathbf{K}}^c = \mathbf{\Psi}^{cT}\mathbf{K}^c\mathbf{\Psi}^c, \quad \bar{\mathbf{f}}^c = \mathbf{\Psi}^{cT}\mathbf{f}^c \tag{2.56}$$

To better understand the derivation of the modes necessary to construct the basis matrix of the reduction (second step), the following partitioning of equation 2.53 will be useful

$$\begin{bmatrix}\mathbf{M}_{ii}\mathbf{M}_{ib}\\ \mathbf{M}_{bi}\mathbf{M}_{bb}\end{bmatrix}\begin{Bmatrix}\ddot{\mathbf{X}}_i\\ \ddot{\mathbf{X}}_b\end{Bmatrix} + \begin{bmatrix}\mathbf{K}_{ii}\mathbf{K}_{ib}\\ \mathbf{K}_{bi}\mathbf{K}_{bb}\end{bmatrix}\begin{Bmatrix}\mathbf{X}_i\\ \mathbf{X}_b\end{Bmatrix} = \begin{Bmatrix}\mathbf{f}_i\\ \mathbf{f}_b\end{Bmatrix} \tag{2.57}$$

and

$$\begin{bmatrix} \mathbf{M}_{ii}\mathbf{M}_{ie}\mathbf{M}_{ir} \\ \mathbf{M}_{ei}\mathbf{M}_{ee}\mathbf{M}_{er} \\ \mathbf{M}_{ri}\mathbf{M}_{re}\mathbf{M}_{rr} \end{bmatrix} \begin{Bmatrix} \ddot{\mathbf{X}}_i \\ \ddot{\mathbf{X}}_e \\ \ddot{\mathbf{X}}_r \end{Bmatrix} + \begin{bmatrix} \mathbf{K}_{ii}\mathbf{K}_{ie}\mathbf{K}_{ir} \\ \mathbf{K}_{ei}\mathbf{K}_{ee}\mathbf{K}_{er} \\ \mathbf{K}_{ri}\mathbf{K}_{re}\mathbf{K}_{rr} \end{bmatrix} \begin{Bmatrix} \mathbf{X}_i \\ \mathbf{X}_e \\ \mathbf{X}_r \end{Bmatrix} = \begin{Bmatrix} \mathbf{f}_i \\ \mathbf{f}_e \\ \mathbf{f}_r \end{Bmatrix} \tag{2.58}$$

The subscripts i, r, e and b denote the interior (not shared with an adjacent component), rigid-body, excess (redundant boundary coordinates) and boundary coordinates, respectively. The number of coordinates are related as follows: $N_b = N_r + N_e$ and $N = N_i + N_b$.

Now concerning the second step, the two main types of component modes that will be developed in this thesis are: the normal modes and constraint modes [24]. These are presented in the following sections.

Normal modes

The normal modes, as it was explained in previous sections, are eigenvectors and they can depend on the interface boundary conditions of the component; this means that there can be: fixed-interface normal modes; free-interface normal modes; or loaded-interface normal modes.

The fixed-interface normal modes can be obtained by restraining all the degrees of freedom and solving the following eigenproblem:

$$\left[\mathbf{K}_i i - \omega_j^2 \mathbf{M}_{ii}\right]\left\{\phi_i\right\}_j = 0, \quad j = 1, 2, ..., N_i \tag{2.59}$$

All the N_i fixed interface normal modes are assembled in the $\mathbf{\Phi}_n$ matrix as follows

$$\mathbf{\Phi}_n = \begin{bmatrix} \mathbf{\Phi_{in}} \\ \mathbf{0}_{bn} \end{bmatrix} \tag{2.60}$$

In the free-interface normal modes case, their derivation consists in solving the eigenproblem presented below

$$\left[\mathbf{K} - \omega_j^2 \mathbf{M}\right]\left\{\phi\right\}_j = 0. \quad j = 1, 2, ..., (N_f = N - N_r) \tag{2.61}$$

This set of modes can be assembled in matrix $\mathbf{\Phi_n}$ as follows

$$\mathbf{\Phi_n} = \begin{bmatrix} \mathbf{\Phi_{in}} \\ \mathbf{\Phi_{bn}} \end{bmatrix} \tag{2.62}$$

Constraint Modes

The definition of the constraint modes comes from the static displacement due to an application of an unit displacement in one of the coordinates, belonging to a set of ”constraint” coordinates. The remaining coordinates of this set are constrained and all the other degrees of freedom are force-free. When this set of coordinates is equal to the set of boundary coordinates the following can be stated

$$\begin{bmatrix} \mathbf{K}_{ii}\mathbf{K}_{ib} \\ \mathbf{K}_{bi}\mathbf{K}_{bb} \end{bmatrix} \begin{bmatrix} \mathbf{\Psi}_{ib} \\ \mathbf{I}_{bb} \end{bmatrix} = \begin{bmatrix} \mathbf{0}_{ib} \\ \mathbf{R}_{bb} \end{bmatrix} \tag{2.63}$$

Thus the constraint mode matrix Ψ_c is formulated as

$$\mathbf{\Psi}_c = \begin{bmatrix} \mathbf{\Psi}_{ib} \\ \mathbf{I}_{bb} \end{bmatrix} = \begin{bmatrix} -\mathbf{K}_{ii}^{-1}\mathbf{K}_{ib} \\ \mathbf{I}_{bb} \end{bmatrix} \tag{2.64}$$

From equation 2.60 and 2.63, it can be concluded that these constraint modes are stiffness-orthogonal to all of the fixed-interface normal modes, thus showing that

$$\mathbf{\Phi}_n^T \mathbf{K} \mathbf{\Psi}_c = \mathbf{0} \tag{2.65}$$

so it can be stated that the set of interface constraint modes $\mathbf{\Psi_c}$ defined by 2.64 will span the static response of the substructure to interface loading and allows for arbitrary interface displacements $\mathbf{u}_b$. Along with this displacements there will be accompanying displacements of the interior of the substructures, determined by 2.64. [24]

Constraint-Mode Method

Now that all the three steps of the CMS method are explained, the tools presented in this section can be used to actually produce the reduced model, thus using the constraint-mode method. This method uses a combination of fixed-interface normal modes and interface constraint modes for the displacement transformation, thus the relation between the full order space and the reduced space can be defined as

$$\mathbf{X}^c = \begin{Bmatrix} \mathbf{X}_i \\ \mathbf{X}_b \end{Bmatrix}^c = \begin{bmatrix} \mathbf{\Phi}_{ik}\mathbf{\Psi}_{ib} \\ \mathbf{0}\mathbf{I}_{bb} \end{bmatrix}^c \begin{Bmatrix} \mathbf{p}_k \\ \mathbf{p}_b \end{Bmatrix}^c \tag{2.66}$$

in which Ψ_{ik} is the interior partition of the fixed-interface modal matrix and Ψ_{ib} is the interior partition of the constraint-mode matrix. Consequently a new reduction basis matrix is derived, the Craig-Bampton matrix, and it can be represented as

$$\mathbf{\Psi}_{CB}^c = \begin{bmatrix} \mathbf{\Phi}_{ik}\mathbf{\Psi}_{ib} \\ \mathbf{0}\mathbf{I}_{bb} \end{bmatrix}^c \tag{2.67}$$

This method has been one of the most popular ROM techniques, because of the simple procedures to formulate the component modes, the straightforward way in which components are coupled, the sparsity patterns of the reduced matrices and because this method also produces highly accurate models [24] [25].

There are many different kinds of modes and methods which are used in the CMS framework, as specified in [24] and [18].

2.2.4 Proper Orthogonal Decomposition

This technique has the main purpose of reducing a large number of interdependent variables to a much smaller number of uncorrelated ones. The main idea is to find a basis, which contains several basis functions, usually referred as proper orthogonal modes (POM). This basis will be the reference for the projection between the physical coordinates and the generalized ones, such that the orthogonal error is minimized (Galerking Projection), with the support of a snapshot matrix.

In order to apply this method, the unknown field $u(\mathbf{x}_n, t)$ has to be considered, where $\mathbf{x}_n$ are the coordinates of the node n of the imposed mesh in a certain domain. The values of $u(\mathbf{x}_n, t)$ are known at the nodes $\mathbf{x}_n$ for the discrete times $t_m = m \cdot \Delta t$, with $n \in [1, ..., M]$ and $m \in [1, ..., P]$. The following notation is used to simplify the mathematical formulation: $u(\mathbf{x}_n, t_m) \equiv u^m(\mathbf{x}_n) \equiv u_n^m$, in which $\mathbf{u}_n^m(\mathbf{x})$ is the vector of nodal values $\mathbf{u}_n$ at time t_m. As it was said before, the main goal of the POD is to derive the already mentioned POMs, such that the orthogonal error is minimized. This problem can be formulated as maximizing the scalar quantity presented below [19]

$$\alpha = \frac{\sum_{m=1}^{P} \left[\sum_{n=1}^{P} \phi(\mathbf{x}_n) u^m(\mathbf{x}_n) \right]^2}{\sum_{n=1}^{M} (\phi(\mathbf{x}_n))^2}, \tag{2.68}$$

this is equivalent to the following eigenproblem

$$\mathbf{c}\boldsymbol{\phi} = \boldsymbol{\alpha}\boldsymbol{\phi} \tag{2.69}$$

in which the vectors ϕ are the POMs with n-component, while α represents the proper orthogonal values (POV) with respect to each POM, the highest values correspond to the modes that best describe the behaviour of the system. Finally the $\mathbf{c}$ matrix is the two-point correlation matrix and can be formulated as

$$c_{ij} = \sum_{m=1}^{P} u^m(\mathbf{x}_i) u^m(\mathbf{x}_j); \quad \mathbf{c} = \sum_{m=1}^{P} \mathbf{u}^m \cdot (\mathbf{u}^m)^T \tag{2.70}$$

It can be shown that the matrix $\mathbf{c}$ is symmetric and positive definite, so it can relate with the snapshot matrix that is defined by

$$\mathbf{Q} = \begin{pmatrix} u_1^1\sqrt{\alpha_1} & u_1^2\sqrt{\alpha_2} & \cdots & u_1^P\sqrt{\alpha_P} \\ u_2^1\sqrt{\alpha_1} & u_2^2\sqrt{\alpha_2} & \cdots & u_2^P\sqrt{\alpha_P} \\ \vdots & \vdots & \ddots & \vdots \\ u_M^1\sqrt{\alpha_1} & u_M^2\sqrt{\alpha_2} & \cdots & u_M^P\sqrt{\alpha_P} \end{pmatrix} \tag{2.71}$$

here α_i are the time integration weights. The snapshot matrix can be just a sample of the time iterations of the HDM solution, or it can even contain all the time iterations. The accuracy of the ROM is supposed to increase with the number of snapshots used in the matrix $\mathbf{Q}$. The relation of the snapshot matrix with the matrix $\mathbf{c}$ can be formulated as

$$\mathbf{c} = \mathbf{Q} \cdot \mathbf{Q}^T \tag{2.72}$$

Then the reduction basis can be defined as

$$\mathbf{B} = \begin{pmatrix} \phi_1(\mathbf{x}_1) & \phi_2(\mathbf{x}_1) & \cdots & \phi_N(\mathbf{x}_1) \\ \phi_1(\mathbf{x}_2) & \phi_2(\mathbf{x}_2) & \cdots & \phi_N(\mathbf{x}_2) \\ \vdots & \vdots & \ddots & \vdots \\ \phi_1(\mathbf{x}_M) & \phi_2(\mathbf{x}_M) & \cdots & \phi_N(\mathbf{x}_M) \end{pmatrix}, \tag{2.73}$$

and the number N of POMs used is equal to the order of the ROM.The usual projection procedure into the generalized coordinate space is applied in a similar manner as all the ROM techniques presented in this section

$$\mathbf{M}_r = \mathbf{B}^T\mathbf{M}\mathbf{B}, \quad \mathbf{K}_r = \mathbf{B}^T\mathbf{K}\mathbf{B}, \quad \mathbf{f}_r = \mathbf{B}^T\mathbf{f} \tag{2.74}$$

always considering the undamped structural HDM used throughout this section, the ROM can be defined as

$$\mathbf{M}_r\ddot{\mathbf{X}}_r(t) + \mathbf{K}_r\mathbf{X}_r(t) = \mathbf{f}_r(t) \tag{2.75}$$

There are several ways of developing the POD, like the ones referenced in [26, 27], nevertheless, the common problem to be solved in this method is mainly concerned with the procedure to solve the eigenproblem presented in 2.68. The three main variants to approach this problem are: Principal Component Analysis (PCA), Karhunen-Loève Decomposition (KLD), Singular Value Decomposition (SVD) [28]. There are also some techniques using AI in the computation of the POD method, more specifically, auto-associative neural networks [29]. Since the only variants that are going to be implemented are the PCA and the SVD, because these are the ones with more relevance and proved application in structural dynamic analysis, the next sections will only focus on these two.

Principal Component Analysis

The main objective of the PCA is to derive the dependence structure behind multivariate stochastic observation in order to obtain a compact description of it. Basically it can also be seen as a least-mean-squares technique [28]. The data presented in the snapshot matrix is already discretized, so the averaged auto-correlation function can be represented by the covariance matrix $\Sigma = E\big[(\mathbf{x}-\eta)(\mathbf{x}-\eta)^T\big]$, in which $\mathbf{E}\big[\cdot\big]$ is the expectation and $\eta = E\big[\mathbf{x}\big]$ is the mean of the vector $\mathbf{x}$. Thus assuming that the process is stationary and ergodic and that the number of time instants is large, a reliable estimate of the covariance matrix is given by the sample covariance matrix [29]

$$\Sigma_S = \frac{1}{n}\begin{bmatrix} \left\{\sum_{j=1}^{n}\left(x_{1j}-\frac{1}{n}\sum_{k=1}^{n}x_{1k}\right)^2\right\} & \cdots & \left\{\sum_{j=1}^{n}\left(x_{1j}-\frac{1}{n}\sum_{k=1}^{n}x_{1k}\right)\left(x_{mj}-\frac{1}{n}\sum_{k=1}^{n}x_{mk}\right)\right\} \\ & \vdots \quad \ddots \quad \vdots & \\ \left\{\sum_{j=1}^{n}\left(x_{mj}-\frac{1}{n}\sum_{k=1}^{n}x_{mk}\right)\left(x_{1j}-\frac{1}{n}\sum_{k=1}^{n}x_{1k}\right)\right\} & \cdots & \left\{\sum_{j=1}^{n}\left(x_{mj}-\frac{1}{n}\sum_{k=1}^{n}x_{mk}\right)^2\right\} \end{bmatrix} \tag{2.76}$$

The POMs and the POVs are then given respectively by the eigenvectors and eigenvalues of the sample covariance matrix Σ_S, like it is proven in [28]. If the sample of the HDM solution has zero mean, the sample covariance matrix is simply given by

$$\mathbf{\Sigma}_S = \frac{1}{n}\mathbf{X}\mathbf{X}^T, \tag{2.77}$$

where $\mathbf{X}$ is the snapshot matrix.

Singular Value Decomposition

Usually the SVD is mentioned as an extension of the eigenvalue decomposition for non-square and non-symmetric matrices, which uses a real factorization that can be formulated as

$$\mathbf{X} = \mathbf{U}\mathbf{S}\mathbf{V}^T \tag{2.78}$$

where the matrix $\mathbf{X}$ can be a random matrix ($m \times n$), in the case of the POD it is the snapshot matrix, while $\mathbf{U}$ and $\mathbf{V}$ are orthonormal matrices containing the left and right singular vectors, respectively. The matrix $\mathbf{S}$ contains the singular values σ_i and is a pseudo-diagonal and semi-positive definite matrix. Knowing that

$$\begin{aligned} \mathbf{X}\mathbf{X}^T &= \mathbf{U}\mathbf{S}^2\mathbf{U}^T \\ \mathbf{X}\mathbf{X}^T &= \mathbf{V}\mathbf{S}^2\mathbf{V}^T \end{aligned} \tag{2.79}$$

it can be concluded that the singular values of $\mathbf{X}$ are the square roots of the eigenvalues of $\mathbf{X}\mathbf{X}^T$ or $\mathbf{X}^T\mathbf{X}$ and the eigenvectors of $\mathbf{X}\mathbf{X}^T$ and $\mathbf{X}^T\mathbf{X}$ are the left and right singular vectors of $\mathbf{X}$, respectively. Therefore the eigenvectors of the sample covariance matrix Σ_s (POMs) are equal to the left singular vectors of $\mathbf{X}$ and the POVs are the singular values σ_i divided by the number of snapshots. In addition this variant also provides relevant information about the model updating of nonlinear systems; this information is given by the right singular vectors [30].

2.2.5 Error estimation and control

Since all methods mentioned above are all based on the derivation of a base, which is responsible for the projection of the physical coordinates in the reduced space of the generalized ones, the error of this process can be given by the total error e_{tot}, which can be decomposed in two components: the

orthogonal error ($e_\perp$) and the colinear error ($e_\parallel$) [2]. Their expressions are presented below.

$$e_{tot} = \mathbf{X} - \mathbf{V}\mathbf{q} = e_\perp + e_\parallel \tag{2.80}$$

$$e_\perp = e_{ortho} = \mathbf{X}(\mathbf{I} - \mathbf{V}\mathbf{V}^T) \tag{2.81}$$

$$e_\parallel = e_{colin} = \mathbf{V}(\mathbf{V}^T\mathbf{X} - \mathbf{q}) \tag{2.82}$$

in which $\mathbf{X}$ is the vector of the HDM variables, $\mathbf{V}$ is the reduction basis and $\mathbf{q}$ is the vector of the ROM variables.

2.3 Other Generalized Coordinate Methods

2.3.1 Least Mean Square Method

The least mean square method comes as an alternative for the Galerkin projection scheme, in which the residual error is orthogonalized with respect to the reduced space [3]. In the case of the least mean square method, rather than projecting the HDM space in such a way that the residual is orthogonalized, the method attempts to minimize the residual error related to the reduction basis, this can be defined for the static model as follows[2]:

$$q = arg\min_q |f(\mathbf{V}\mathbf{q})|, \tag{2.83}$$

where V is the reduction basis and q is the displacement vector of the HDM. With this being said, the reason why all the previous methods used the Galerkin projection as the link between the full order space and the reduced one is because most of the literature, that presents their respective formulations, use the Galerkin projection most of the time. Just in some few exceptions was the least mean square preferred to the projection alternative, when it comes to structural analysis, like in the POD developed in [2] and [31], where the POD (SVD variant) is applied with least mean square instead of using Galerking projection. As it was cited in [2], for dynamical analysis the POD with least mean square scheme is likely to be dissipative and stable [32], on the other side, the POD using the Galerkin projection scheme can generate unstable models [33]. The Matlab least mean square solver algorithm is analytically equivalent to the standard method of conjugated gradients and it can be found in [34] and it will be the one used in the benchmarks presented in chapter 3.

2.3.2 Proper Generalized Decomposition

In this section a brief description of the recently developed *a priori* method for MOR called the Proper Generalized Decomposition (PGD) will be made. Starting by considering the unknown field $u(x_1, \cdots, x_D)$, the variables x_i usually represent the coordinates related to the physical space or time, but in this case they can also represent other parameters like boundary conditions or material parameters as described

in [35]. The PGD has as the main goal finding a solution for

$$u^N(x_1, \cdots, x_D) = \sum_{i=1}^{N} F_i^1(x_1) \times \cdots \times F_i^D(x_D) \tag{2.84}$$

wherein N and F_i^j are the number of approximation terms and functions, respectively. So the PGD approach 2.84 can be seen as a sum of N functional products, each with a number D of functions $F_i^j(x_j)$ that are unknown a priori. This method is solved by using enrichment steps, which are responsible for the sequential derivation of each functional product. Basically at each enrichment step $n+1$, the functions F_{n+1}^j are already known due to their derivation in the previous steps, so in this enrichment one must determine the new product involving the D unknown functions $F_{n+1}^j(x_j)$. This can only be accomplished by deriving the weak formulation of the model. Another achievement of the PGD is the considerable decrease on the unknowns of the original problem, since without the technique the number of degrees of freedom are given by M^D and with the PGD, the number of unknowns are reduced to $N \times M \times D$, thus avoiding the exponential complexity of the usual FEM problem. These method has had recent developments in its applicability to structural analysis and the FEM, as it is shown in [35], [36] and [37].

2.4 Hybrid Coordinates

The hybrid reduction methods are still a area of study that does not have that much development, but there are some research done proving the applicability of these techniques, for example, considering the static condensation that is applied to the slave degrees of freedom and then a reduction in the modal space is applied to the master degrees of freedom [38]. This kind of methods can also be seen applied to the CMS variants, when both kinds of interfaces are used (fixed and free interfaces) [9]. There is also a hybrid reduction method involving substructuring and the POD technique [39]. Since the implementation of this thesis will only involve the methods using the physical and generalized coordinates, no further extension of the hybrid methods will be made here, but the references cited are left for future work.

Chapter 3

Benchmark Reduction

3.1 Introduction

The following chapter of this thesis will explore the implementation of the methods introduced in chapter 2. This implementation will consist in testing the accuracy of the referred techniques on structural benchmark models taken from [40], which is an online website dedicated to MOR where the community can exchange ideas and test cases. These models will consist in the typical dynamical equations of equilibrium, recurrently mentioned on the formulations of the MOR techniques presented in the previous chapter; these include the mass, damping and stiffness matrices. The data of the models are given in Matrix Market format, allowing for the dynamic simulation of the systems.

The methods that will be tested are:

- Condensation method
- Mode displacement method
- Static Ritz vector method
- POD-Galerkin Projection (PCA variant)
- POD-Galerkin Projection (SVD variant)
- POD-Least Mean Squares (SVD variant)

In order to determine the specific characteristics of each one of the methods, there will be different types of time intervals that will be taken into account. They are enumerated and defined as follows:

- Sample time - Defined by the duration of the sampling phase of the method in question. Only valid for POD variants, because of their *a priori* formulation.
- Selection time - Time interval only valid for the condensation method, where the master and slave degrees of freedom are chosen.
- Basis time - Consists in the time duration relative to the derivation of the reduction basis.

- Solve time - Measures the time period related to the actual solving process of the equations obtained in the ROM.
- Reduction time - Time interval where the reduced matrices are derived.
- Total time - Consists in the aggregation of all the time intervals mentioned before.

Other parameters of interest will be the errors introduced in the ROM, when compared with the HDM. In the case of the condensation and the POD - Least Mean Square the only error that is considered will be the relative output error, which is the relative error between the values of the HDM and the ROM solutions, consequently defined by

$$e_{out} = \frac{|\mathbf{q}_{HDM} - \mathbf{q}_{ROM}|}{|\mathbf{q}_{ROM}|} \tag{3.1}$$

in which the $\mathbf{q}_{HDM}$ and $\mathbf{q}_{ROM}$ are the HDM and ROM solutions, respectively.

Another benchmark parameter is the relative time reduction, which consists in the following formulation:

$$t_r(\%) = \frac{t_{HDM} - t_{ROM}}{t_{HDM}} \times 100, \tag{3.2}$$

where the t_{HDM} and t_{ROM} are the HDM and ROM total computation time, respectively.

For the projection based generalized coordinate methods the output error will also be taken into account, as well as the orthogonal, colinear and total errors, which were described in the last chapter. These errors do not apply to the condensation and least mean square methods, because no projection is made.

The order of the ROM will be another object of study; since the higher the order of the model the highest the accuracy will be; however the solving time will also be increased. In the case of the POD variants, another critical fact is the number of snapshots that needs to be considered, that is, how many time step solutions of the HDM need to be sampled, so that the POD model becomes reasonably precise (output error approximately less than 5%).

The benchmarks that are going to be used in the next sections of this chapter are:

- Butterfly Gyroscope [41]
- Circular Piston [42]
- Car Windscreen [43]

To have a better notion of the size of these models and since the main goal of this thesis is to apply these MOR methods to an aircraft structure, having a reference of the size of an actual structural HDM model of an aircraft could be of great use. The structural design report of the Lockhead-Martin F-35 [44] includes the dimensions of the HDMs used in its design, which were reported to have an approximate number of 117000 nodes in its simplest variant, for the entire structure. If it is assumed that each node has 6 degrees of freedom, which is the standard number for a 2-D mesh computed using commercial FEM software; the dimension of the model will be equal to 702000. Computing models with dimensions in the order of magnitude of the hundred of thousands in a laptop is completely unrealistic. Bearing this

in mind, the size of the Butterfly Gyroscope and Car Windscreen benchmarks are in the order of the tens of thousands of degrees of freedom, which can already give a good idea of the time reduction due to the MOR techniques.

All the enumerated benchmarks take into consideration the damping effects of their structures, but since the damping effects are usually a minor issue in a dynamic structural analysis, and since the MOR methods presented previously also neglect these effects, the following analysis will also ignore them, but always bearing in mind that the results will have an error introduced by this assumption. The solver used in the numerical simulation was the Newmark-β method presented in [45] and verified in [2].

All the computations were made using Matlab, with a laptop with an Intel Core i7-6700HQ CPU with a frequency of 2.6 GHz, a RAM memory of 16.0 GB and running Windows10 as its operative system.

3.2 Butterfly Gyroscope

3.2.1 Introduction and Applied Methods

The system that will be firstly analyzed is the Butterfly Gyroscope, which has been developed by Imego Institute in a project with Saab Bofors Dynamics AB. This system is used in micro electro-mechanical systems (MEMS) and it consists of a vibrating micro-mechanical gyro that has a potential to be used in inertial navigation applications. The data given in [41] was generated by modelling and semi-discretizing the system in Ansys, resulting in the form:

$$\mathbf{M}\ddot{\mathbf{x}} + \mathbf{E}\dot{\mathbf{x}} + \mathbf{K}\mathbf{x} = \mathbf{b}u, \tag{3.3}$$

in which u is the nodal force applied at the centers of the excitation electrodes and can be represented as:

$$u = 0.055\text{sin}[2384(\text{Hz}) \times t] \quad (\mu\text{N}) \tag{3.4}$$

where $\mathbf{b}$ is the load vector, which contains unitary values in the positions respective to the degrees of freedom of the nodes at which the nodal force is applied.

One problem with this benchmark is that the units of the matrices are not given, so it was assumed that they were derived in μm, since the unit presented in the nodal force is the μN. In all the simulations presented here, the initial conditions of all the variables were set to be null. The time interval chosen is defined by $t \in [0; 3 \times 10^{-3}](s)$ and the time step is equal to $1 \times 10^{-4}(s)$. As it was stated in the introduction of this chapter, the damping of the model will be neglected, so the actual HDM that will serve as a reference in this benchmark has the following form

$$\mathbf{M}\ddot{\mathbf{x}} + \mathbf{K}\mathbf{x} = \mathbf{B}u. \tag{3.5}$$

The difference between the undamped and damped systems can be easily seen in figure 3.1. The time

duration necessary to compute the undamped model is 563.461 seconds.

This benchmark will focus on the implementation of the POD methods, not only in the Galerkin projection scheme, but also with the least mean square alternative. Therefore the methods that will be applied here are the:

- POD - Galerkin Projection (PCA variant);
- POD - Galerkin Projection (SVD variant);
- POD - Least Mean Squares (SVD variant);

Having a benchmark focused only on the POD method will ease the analysis of the results, since it is the only method where snapshots are needed. Therefore, having this focus will simplify the study of the influence of the number of snapshots and the order of the ROMs in the accuracy of the solutions obtained by the MOR methods.

This benchmark was also used in [2], but the only method implemented there was the SVD variant of the POD in the Galerkin projection scheme. In this thesis the other alternatives of the POD are going to be explored as well, with the goal of comparing their performance.

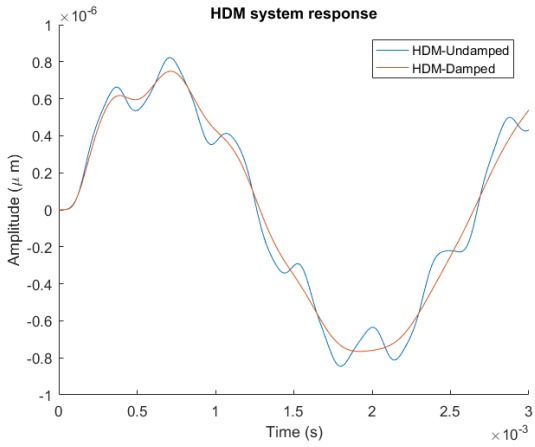

Figure 3.1: Damped and undamped HDM response.

3.2.2 Results and Discussion

Before beginning the discussion of the results, it must be mentioned that the snapshot study will consist in varying the number of snapshots taken from the HDM solution. Thus the snapshots will have an equally spaced distribution, with a spacing of ΔS, with respect to the time iterations.

Error estimation and analysis

An error estimation of the POD methods in the Galerkin projection scheme will be made for each ΔS, where the evolutions of the orthogonal, colinear and total error are analyzed in respect to the ROM order, with the main purpose of concluding which parameters (ΔS and ROM order) give the most accuracy to

each projection based MOR method. The results for POD-SVD and POD-PCA methods considering $\Delta S = 1$ and $\Delta S = 5$ are presented in figures 3.2, 3.3, 3.4 and 3.5.

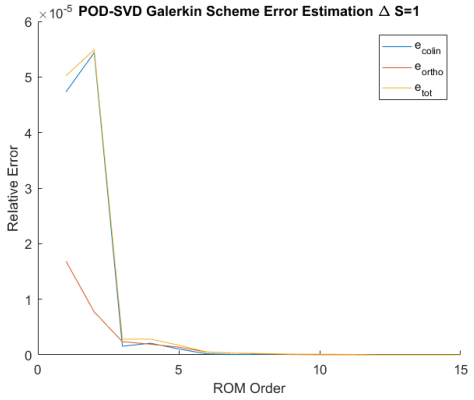

Figure 3.2: Error Estimation for the POD-SVD in the Galerkin Projection Scheme with a snapshot spacing of $\Delta S = 1$.

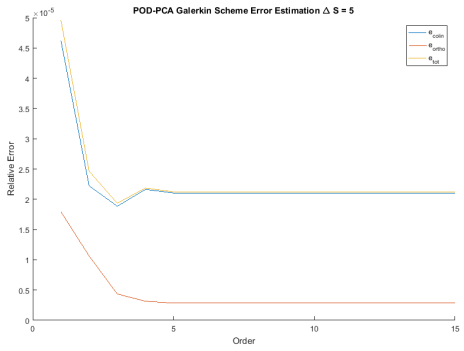

Figure 3.3: Error Estimation for the POD-PCA in the Galerkin Projection Scheme with a snapshot spacing of $\Delta S = 5$.

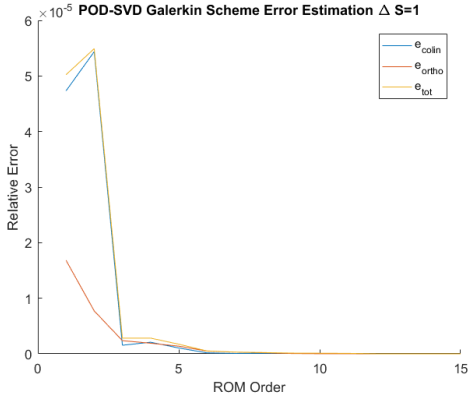

Figure 3.4: Error Estimation for the POD-SVD in the Galerkin Projection Scheme with a snapshot spacing of $\Delta S = 1$.

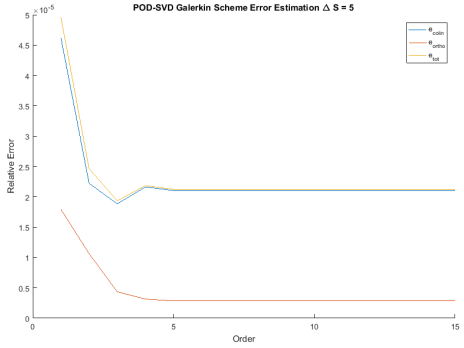

Figure 3.5: Error Estimation for the POD-SVD in the Galerkin Projection Scheme with a snapshot spacing of $\Delta S = 5$.

From figures 3.2, 3.3, 3.4 and 3.5 it can be drawn that the error behaviour for each variant is similar, as well as their error values when these are stabilized, that is, when they both converge to a total error value lower than 2.12×10^{-5}, in the case of the snapshot spacing of $\Delta S = 5$ and 2.74×10^{-11} for the snapshot spacing value of $\Delta S = 1$.

The relative output error consists in comparing the solution of the HDM with the ROMs solutions, including the POD variant where the least mean square serves as an alternative to the Galerkin projection. This relative output error estimation is presented graphically in the figures 3.6 and 3.7, for three POD methods and two snapshot spaces ($\Delta S = 5$ and $\Delta S = 1$, respectively).

The relative output error graphics demonstrate the increase in accuracy along with the increase of the number of snapshots used. The same observation is verified for the ROM's order relatively to the accuracy of the reduced solution. These two remarks can be drawn for all the POD variants studied in this benchmark.

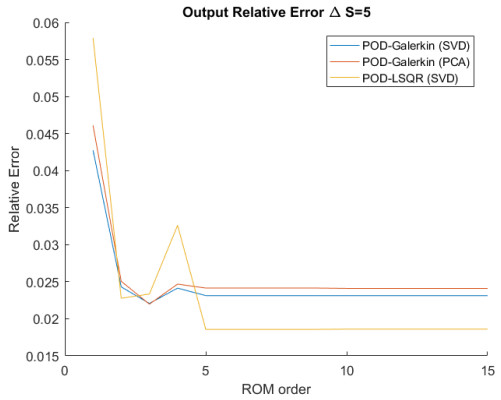

Figure 3.6: Output Error Estimation with a snapshot spacing of $\Delta S = 5$.

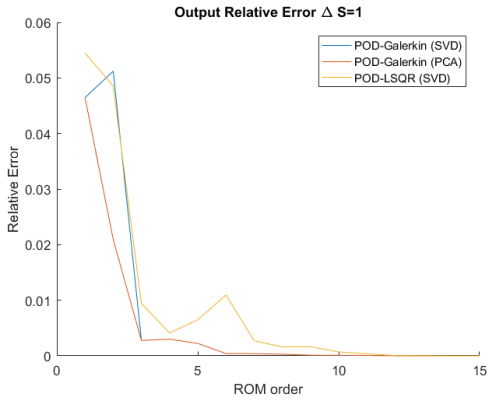

Figure 3.7: Output Error Estimation with a snapshot spacing of $\Delta S = 1$.

It has to be highlighted that for the case of $\Delta S = 5$, all methods stabilize with the same order, but the most accurate method is the POD-SVD using the least mean square method. However when ΔS is increased, both POD variants with the Galerkin projection scheme stabilize with a smaller order comparing to the least mean square, which turns out to have a similar accuracy, but only obtained with a larger order.

Time duration analysis

In the case of the POD, there will be a component of the total time that will be related to the duration of the sampling process. This time interval will only depend on the size of the snapshot space ΔS, as shown in table 3.1. It can be concluded that the sample time does not have a significant impact on the total time, but if the HDM solution includes more time iterations, consequently imposing the possibility of taking more snapshots from the solution, or if there is a sampling method involved with the purpose of decreasing the error, like the ones mentioned in [2], these factors could increase the sampling time significantly.

ΔS	Sample time (s)
1	0.003
5	0.002
10	0.001

Table 3.1: Sample time for all the ΔS values.

The basis time will depend on the basis derivation method chosen and on the value of the snapshot spacing ΔS. It can be established from table 3.2, that the SVD option is significantly more influenced by the parameter ΔS in comparison to the PCA method. Consequently the PCA has a better time performance for a higher number of snapshots used, when compared to the SVD; on the other hand for a low number of snapshots, the SVD has a small advantage over the PCA.

The actual solver chosen to derive the ROM solution is different depending on the choice between the Galerkin projection or the least mean square option, because in the case of the Galerkin scheme,

ΔS	PCA(s)	SVD(s)
1	3.762	11.342
5	3.858	3.045
10	3.573	2.154

Table 3.2: Basis time for all ΔS and basis methods used.

the typical Matlab Cholesky solver can be used, on the other hand, the least means square method has its own solver on Matlab [34]. The time duration of the solving process, for both these solvers, is dependent on the order of the ROM. Their relation is presented in figure 3.8, where it can be noticed that the least mean square solver is much more influenced by the order of the ROM than the Cholesky solver.

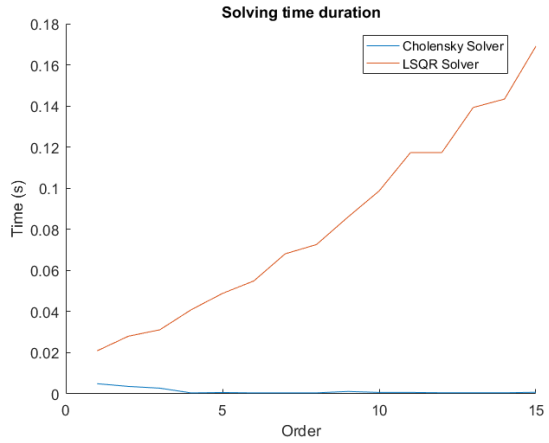

Figure 3.8: Solving time relation with the ROM order

Since the Galerkin projection and the least mean square method have different approaches when deriving the reduced matrices and due to the dependency of the reduction time interval in relation to the ROM's order, the graphic presented in figure 3.9 shows the different evolution of this time interval for both methods. It can be established that the reduction time for the Galerkin projection scheme is more likely to vary with the order of the ROM, when compared to the least mean squares method, which does not have a major variation in the reduction time.

After the error and time analysis, a direct comparison between the solutions of the reduction methods and the HDM is presented. The order of the reduced solutions presented in the following tables are the ones respective to the ROM from each MOR technique, in which the output error first stabilizes, for both $\Delta S = 1$ and $\Delta S = 5$. Therefore, the ROMs obtained with the SVD and PCA variants of the POD-Galerkin, correspond to an order of 6 and the POD using the least mean square variant will have an order equal to 10. This criteria of choosing the order of the ROMs was chosen because the parameter with more relevance in this analysis is the accuracy, thus the resulting solutions will have, as a fundamental aspect, the guaranteed accuracy of the reduced solutions.

The time analysis of the respective ROMs are presented in tables 3.3 to table 3.5 and their solution is graphically represented in figures 3.10 and 3.11. It can be concluded from these tables that for

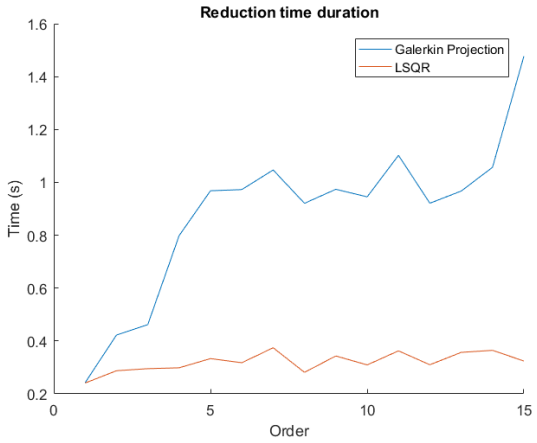

Figure 3.9: Reduction time relation with the ROM order

all the MOR methods tested the relative time reduction is above 95%. One should bear in mind that the accuracy criteria, used in this analysis, guarantees relative output errors below 1%. It can also be noticed that the only time duration with considerable order of magnitude is the basis time. Since measuring time in computational simulations is very relative, even if all the simulations are tested in the same machine and specially when the time intervals measured are in the order of the millisecond, therefore the accuracy can not be assured for these time intervals. Nevertheless, a general behaviour of the computation time can be drawn from the results.

ΔS	Sample time(s)	Basis time(s)	Reduction time(s)	Solve time(s)	Total time(s)	t_r (%)
1	0.003	11.342	0.0005	0.474	11.820	97.547
5	0.002	3.045	0.0005	0.474	3.522	99.020

Table 3.3: Time analysis for the sixth order ROM obtained via POD-Galerkin (SVD)

ΔS	Sample time(s)	Basis time(s)	Reduction time(s)	Solve time (s)	Total time(s)	t_r (%)
1	0.003	3.762	0.0005	0.474	11.820	97.547
5	0.002	3.858	0.0005	0.474	4.3345	98.879

Table 3.4: Time analysis for the sixth order ROM obtained via POD-Galerkin (PCA)

ΔS	Sample (s)	Basis time(s)	Reduction time(s)	Solve time(s)	Total time(s)	t_r (%)
1	0.003	11.342	0.152	0.344	11.841	97.544
5	0.002	3.045	0.152	0.344	3.543	99.016

Table 3.5: Time analysis for the tenth order ROM obtained via POD-LSQR (SVD)

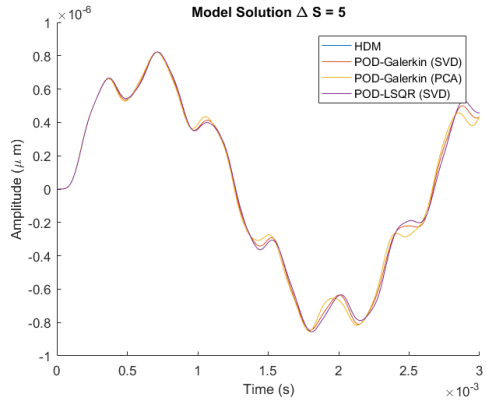

Figure 3.10: Gyroscope system response for $\Delta S = 5$

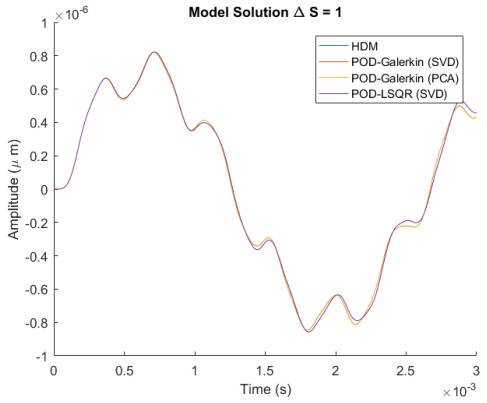

Figure 3.11: Gyroscope system response for $\Delta S = 1$

3.3 Circular Piston

3.3.1 Introduction and Applied Methods

The next benchmark is not a structural model by definition, since it consists of an acoustic radiation analysis discussed in [42]; however its formulation is based on the equilibrium equations in which all the MOR methods have been developed in this thesis, that is:

$$\mathbf{M}\ddot{\mathbf{x}} + \mathbf{E}\dot{\mathbf{x}} + \mathbf{K}\mathbf{x} = \mathbf{f}, \tag{3.6}$$

with $\mathbf{f}$ being the input vector of the system.

The domain of this model is axi-symmetric and divided in an inner and outer domain. The inner domain is discretized using a mesh of linear rectangular finite elements and the outer domain adopts conjugated infinite elements of order 5. According to the reference of this benchmark the initial conditions of the model variables were all set to null, the matrices and the input vector of equation 3.6 were computed in SI units using Free Field Technologies, which is a simulation software for structural analysis. All simulations made in this benchmark had in consideration the time interval: $t \in [0; 3 \times 10^{-3}](s)$ and the time step is equal to $1 \times 10^{-5} s$.

The computation time and the response of the system are shown in table 3.6 and figure 3.12, respectively.

Model	Computation time (s)
HDM	40.500

Table 3.6: Necessary computation time for the undamped HDM solution.

This model has 2025 degrees of freedom, being the smallest benchmark of this chapter. This is why the MOR techniques applied here are the ones which were predicted to require more computation time and RAM memory. This way they can be tested more efficiently, otherwise an impracticable amount of time would be required or could not even be run, due to insufficient RAM memory.

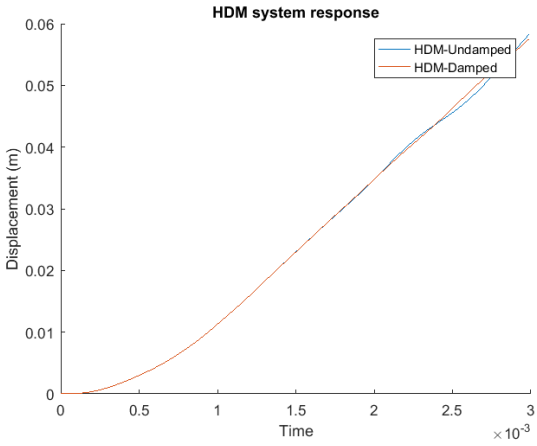

Figure 3.12: Damped and undamped HDM response.

Since there were not found any benchmark models which supplied enough information, like grid point coordinates or any geometric characteristics of the domain, the CMS method could not be applied in this thesis. Therefore the other methods presented in 2 and not implemented in the last section are now applied in this benchmark. These methods are:

- Mode displacement method;
- Static Ritz vector method;
- Condensation method.

The performance analysis of these three methods will begin by an error estimation of their solution, followed by the analysis of the time intervals needed by the methods to have an accurate solution. Here the damping of the system is ignored, like the previous example, thus re-defining the model as follows:

$$\mathbf{M}\ddot{\mathbf{x}} + \mathbf{K}\mathbf{x} = \mathbf{f}. \tag{3.7}$$

3.3.2 Results and Discussion

In the case of these three MOR methods the use of snapshots is not necessary, so their analysis will consist only in the study of the evolution of the error and time intervals in relation to the order of the ROM, except for the condensation method, which does not have any parameter responsible for the determination of its order. So in this last case (condensation method), the error and time analysis will have no relation to the order, but their respective definition and outcome will be clarified in this section.

Error estimation and analysis

The total error estimation concerning the projection of the HDM, using the Ritz vectors (Static Ritz vector method) and the free vibration modes (Mode displacement method), is ploted in figures 3.13 and 3.14, respectively.

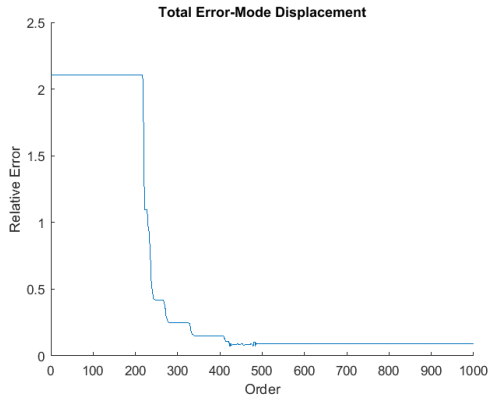

Figure 3.13: Total error of the solution corresponding to the mode displacement method

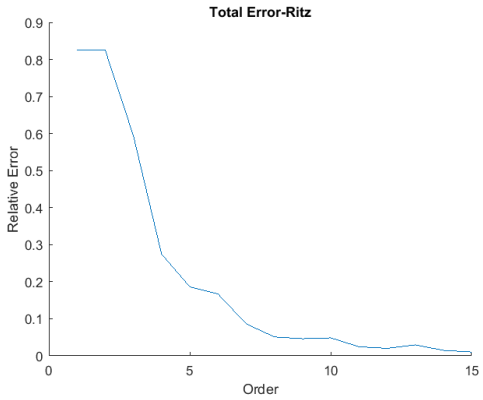

Figure 3.14: Total error of the solution corresponding to the static Ritz vector method

The first conclusion that can be drawn from these figures concerns the magnitude of the ROM order needed for the mode displacement method to stabilize its total error. The mode displacement method needs to have a ROM order approximately equal to 420 to have a stabilized total error with a value of around 8%. On the other hand the static Ritz vector method needs a much smaller ROM order so that its total error is kept approximately constant; in addition to that, the total error attained is around 1%. Comparing these total errors with the ones obtained in the previous benchmark, where the POD variants were developed, the optimal characteristics of the POD are evidenced, since it just needs 1 or 2 POMs to have a much smaller total error.

The relative output error can be analyzed in figures 3.15 and 3.16. The relative output error from both methods stabilize in values which give the ROMs a satisfactory accuracy, that is, for the static Ritz method the error stabilizes approximately with a value of 1% and in the case of the mode displacement method the error stabilizes approximately at 0.0001%. However, in relation to the mode displacement method, it can be easily seen that the method needs a much bigger basis, when compared to the basis used in the stabilized Static Ritz method, which can become penalizing when it comes to the basis time of the respective MOR technique.

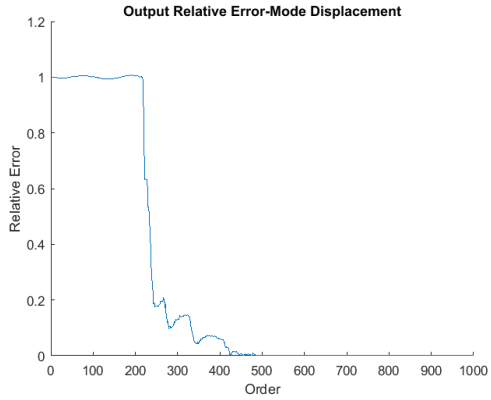

Figure 3.15: Relative output error of the solution corresponding to the static Ritz vector method

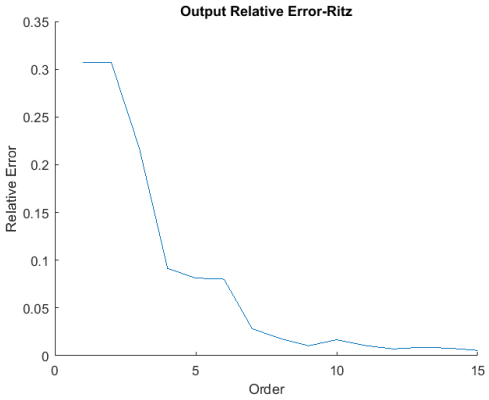

Figure 3.16: Relative output error of the solution corresponding to the mode displacement method

The condensation method, in the case of this benchmark, defines the masters as the degrees of freedom corresponding to the ones where the force is applied, consequently there will be 11 degrees of freedom considered as masters and the remaining as slaves. In this scheme the relative output error obtained for this method was approximately equal to 38.05%.

Time duration analysis

For the static Ritz vector method and the mode displacement method, the time intervals, which measure the steps of their procedure are: the basis time, reduction time and solve time. For the Ritz method the only time with relevant magnitude is the basis time. The same cannot be said for the mode displacement method, where the solve time and the basis time have significant impact on the total time duration of the method. In the case of the condensation method there is no basis time, but another kind of time interval needs to be introduced, the selection time; its definition was explicited in the introduction of this chapter.

The first analysis that will be addressed is the only relevant time interval in common between the Ritz and mode displacement methods, that is the basis time. It can be seen from table 3.7 that the basis time is much larger for the mode displacement method; this is due to the fact that for this method all the eigenvectors, corresponding to the free vibration modes, need to be derived and this procedure penalizes time and RAM memory performance. The derivation of just some specified number of eigenvectors was attempted with a specific function of Matlab called *eigs*, but with a drastic decrease in the accuracy of the ROM. It was then concluded that all the free vibration modes needed to be derived, so that the truncation error of the Matlab function would not interfere with the accuracy of the method.

	Static Ritz vector	Mode displacement
Basis time (s)	2.981	57.100

Table 3.7: Time intervals respective to the reduction basis derivation of the static Ritz vector method and the mode displacement method.

The solving time has a significant weight in the time performance only for the mode displacement method, since for the other two MOR techniques the solve time is in the order of magnitude of the milisecond. The figure 3.17 represents this time interval evolution relative to the order of the mode displacement method. It can be confirmed that the solve time for a reasonably accurate ROM (relative output error around 1%) has, at least, a solve time close to 4 seconds.

Similarly to what was done at the end of the last benchmark, a direct comparison of the time performance of each MOR method is going to be presented. The results are shown in table 3.8 and their solution is represented in figure 3.18. The solution obtained by the static Ritz vector ROM is given for an order of 15, corresponding to a relative output error of 0.5%. The ROM's solution derived by the mode displacement method has an order of 480, also having a relative output error of 0.5% too.

From tables 3.8 and 3.9, it is evident that the static Ritz vector method is the one with the largest relative time reduction, followed by the condensation method. Due to the excessive basis time, the mode displacement method needs even more time than the HDM to compute its solution, this could be avoided if the number of eigenvectors was known *a priori* and without the error associated with the truncation

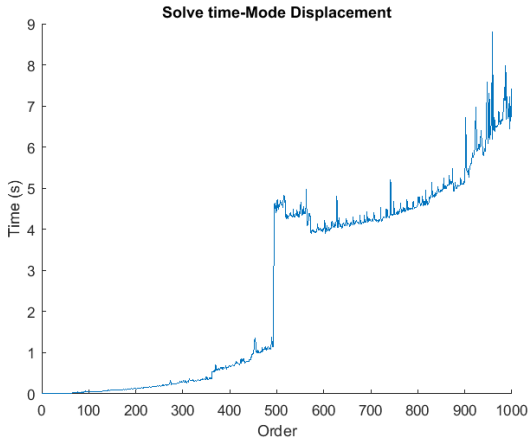

Figure 3.17: Solve time behaviour relative to the mode displacement ROM order

Method	Selection time(s)	Basis time(s)	Reduction time(s)	Solve time(s)	Total time(s)
Static Ritz vector	-	2.981	0.009	0.005	2.996
Mode Displacement	-	57.100	0.005	2.592	59.697
Condensation	2.967	-	0.291	0.008	3.266

Table 3.8: Time performance comparison respective to all methods applied in this section

algorithm of the Matlab function mentioned before. Another remark that needs to be highlighted is the high inaccuracy of the condensation method, even though its relative time reduction is above 90%, the method fails to be accurate when compared to the other alternatives, at least for this specific model.

Methods	t_r (%)	e_r (%)
Static Ritz vector	92.603	0.5
Mode displacement	-	0.5
Condensation	91.936	38.05

Table 3.9: Relative time reduction and relative output error for each method applied in this section

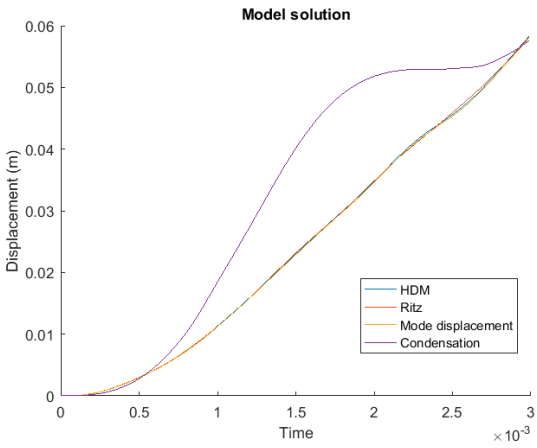

Figure 3.18: HDM and ROM solutions

3.4 Windscreen

3.4.1 Introduction and Applied Methods

In the following section a structural model of a windscreen is going to be analyzed. All the data and description of this model can be consulted in [43]. A particular fact about this model is that it is defined in the frequency domain, so instead of the typical model equilibrium equation, the model will be defined by:

$$(\mathbf{K}_d + \omega^2 \mathbf{M})\mathbf{X} = \mathbf{f}, \tag{3.8}$$

where $\mathbf{K}_d = (1 + i\gamma)\mathbf{K}$, with $\gamma = 0.1$, which represents the natural damping factor. The complex part of the stiffness matrix $\mathbf{K}_d$ represents the damping of the structure. Because of the general assumption made in this thesis, the damping will be neglected and the model will be formulated as:

$$(\mathbf{K} + \omega^2 \mathbf{M})\mathbf{X} = \mathbf{f}, \tag{3.9}$$

where $\mathbf{K}$ is the stiffness matrix, $\mathbf{M}$ is the mass matrix, $\mathbf{X}$ is the displacement and $\mathbf{f}$ the force vector. Even though all the MOR method formulations were made using models in the time domain, the implementation in the frequency domain should be analogous.

This is a 3D problem with a dimension of 22692 degrees of freedom. The discretization of the model was made using a mesh composed of hexagonal elements (3 layers of 60×30). The structural boundaries are free and the force vector represents a unit point load applied at a corner. All the computations were made in the frequency interval $\omega \in [0.5; 200]$ (rad/s) and the frequency step was equal to $0.5\ rad/s$. [46]

The damped and undamped solution of the HDM is represented in figure 3.19 and the total time for its computation is shown in table 3.10.

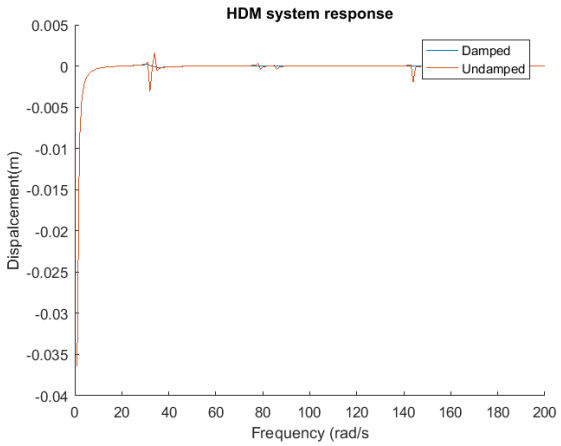

Figure 3.19: Damped and undamped HDM response.

In this benchmark, a general error and time performance analysis will be made, comparing the relative output error and total time of all the methods implemented in chapter 3. After that, a parametric analysis will be made with the purpose of knowing the adaptability of the ROMs derived by the MOR

Model	Computation time (s)
HDM	388.034

Table 3.10: Necessary computation time for the undamped HDM solution.

methods, when the force vector is changed. This can be useful to draw conclusions on the suitability of the MOR techniques when parametric studies are needed, in particular when several analyses are made, focusing on the type of loads that a certain structure needs to withstand.

3.4.2 Results and Discussion

Error and time performance analysis

The first analysis made in this benchmark consists in comparing the evolution of the output relative error of each method in relation to the ROMs's order. This can be seen in figure 3.20. The snapshot spacing was defined based on the values that provide more accuracy: $\Delta S = 5$ for the POD ROMs with the Galerkin projection scheme; and $\Delta S = 20$ for the least mean square ROMs. It can also be seen that for the least mean square POD the error does not have an appropriate convergence for this kind of study, since the error increases when 7 or more POMs are used.

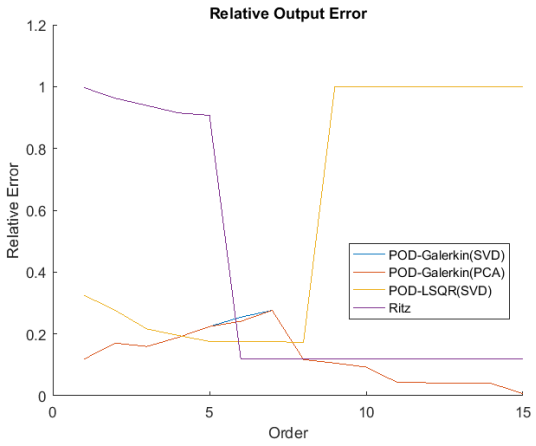

Figure 3.20: Relative output error evolution in relation to the ROMs's order.

The condensation method did not render any accurate results (relative absolute error above 100%), in addition to the excessive magnitude of the value corresponding to the selection time, reaching a value above one hour. There were also problems with the implementation of the mode displacement method, since the memory of the computer used was not enough to derive all the eigenvectors needed for this method.

Parametric analysis

The following parametric analysis will consist on studying the behaviour of a ROM when the force vector solicited on it is not the one which was used in its formulation, for example, the POD ROMs which are

used in this study were formulated using the snapshots of a solution which used the original force vector given by this benchmark, but in this analysis, these same models will have different force vector as their solicitation. With this variation, conclusions can be drawn on the ROM's adaptability to different force vectors.

For the case of the Galerkin projection based POD methods, the order chosen was equal to 15 and $\Delta S = 5$. For the least mean squares variant, the parameter values chosen were 6 for the order of the ROM and 20 for the snapshot spacing. In the static Ritz vector method the order chosen was equal to 15. These values were defined considering an error analysis (carried out previously) and aiming at the highest accuracy possible for the reduced solution. It is important to note that the ROMs derived with each MOR technique will be the same in the several simulations of this parametric study, that is why the basis time will only be a component of the total time for the derivation of the ROM, since the creation of the reduction basis will only be needed to construct the ROM in the first place.

The force vector will vary throughout this parametric analysis in three case studies. In the first case the original force vector of the HDM is used. The time performance and error estimation of the methods are shown in table 3.11.

Methods	total time (s)	t_r (%)	e_r (%)
POD-Galerkin (SVD)	46.144	88.1	0.7
POD-Galerkin (PCA)	7.037	98.2	0.7
POD-LSQR (SVD)	7.215	98.1	17.3
Ritz	3052.440	-	11.9

Table 3.11: Relative time reduction and relative output error in respect to the model with the original force vector

In the second case the force vector will maintain the direction and the node of application, the only change will be in its magnitude, which is now 100 N. The results of the ROMs's performance are stated in table 3.12.

Methods	total time (s)	t_r (%)	e_r (%)
POD-Galerkin (SVD)	0.036	99.9	0.7
POD-Galerkin (PCA)	0.034	99.9	0.7
POD-LSQR (SVD)	0.034	99.9	47.2
Ritz	0.176	99.9	17.6

Table 3.12: Relative time reduction and relative output error in respect to the model with the force vector with a magnitude of 100 N

In the third case all the properties of the force vector will remain the same, except for the magnitude, which will have a value of 1000 N. The time and error analyses is shown in the table 3.13.

In what concerns the error estimation of this parametric analysis, it can be concluded from tables 3.11, 3.12 and 3.13 that the error remains practically the same in relation to the original model, except for the least mean square POD variant, for which the error increases for more than its double, when a different force magnitude is used.

Methods	total time (s)	t_r (%)	e_r (%)
POD-Galerkin (SVD)	0.053	99.9	0.7
POD-Galerkin (PCA)	0.045	99.9	0.7
POD-LSQR (SVD)	1.181	98.1	47.23
Ritz	0.417	99.9	11.86

Table 3.13: Relative time reduction and relative output error in respect to the model with the force vector with a magnitude of 1000 N

In table 3.11, 3.12 and 3.13 it can also be noticed that the relative time reduction increased in the two cases where the ROM was already derived (case with force magnitudes of 100 and 1000 N). Since the basis was derived with the original force vector, in these two cases there will be no basis, sampling or reduction times, therefore the total time will be equal to the solve time. This is simply because the ROM was already formulated in the first case.

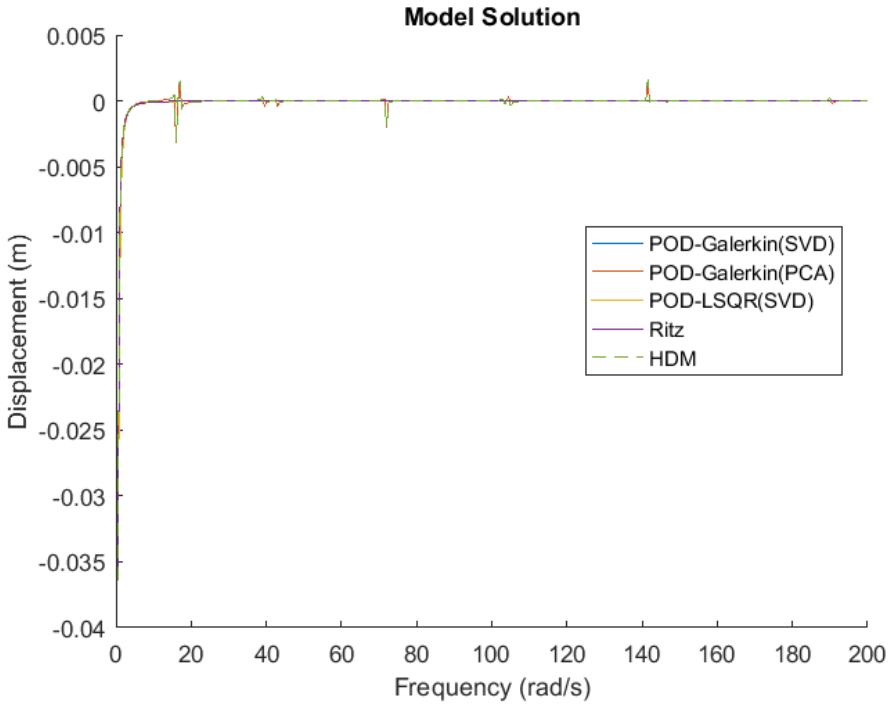

Figure 3.21: HDM and ROM solution corresponding to the original force vector.

The responses of the ROMs and HDM corresponding to the three cases of the parametric analysis are presented in figure 3.21, 3.22 and 3.23.

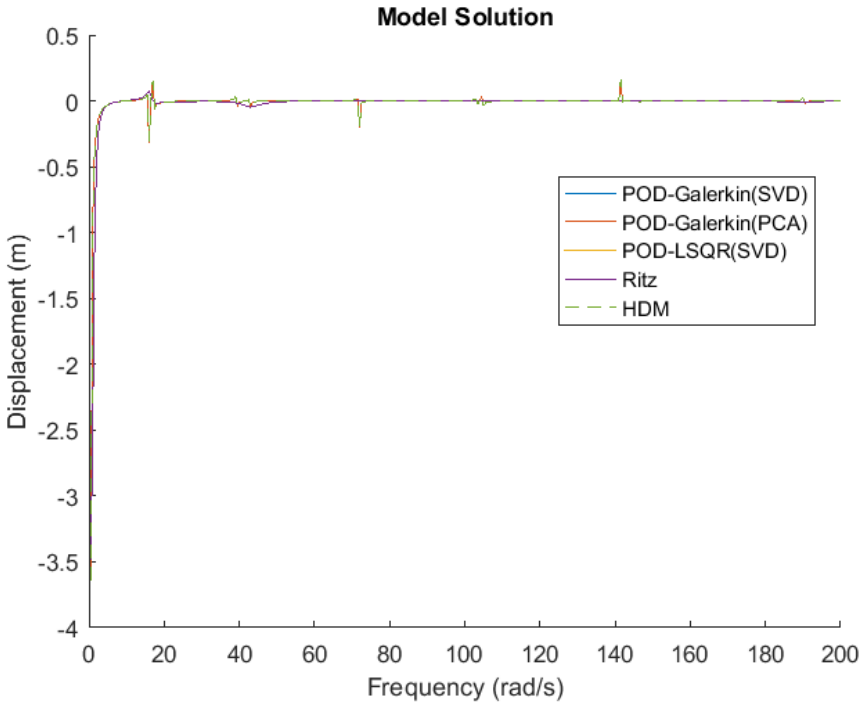

Figure 3.22: HDM and ROM solution corresponding to the force vector with 100 N of magnitude.

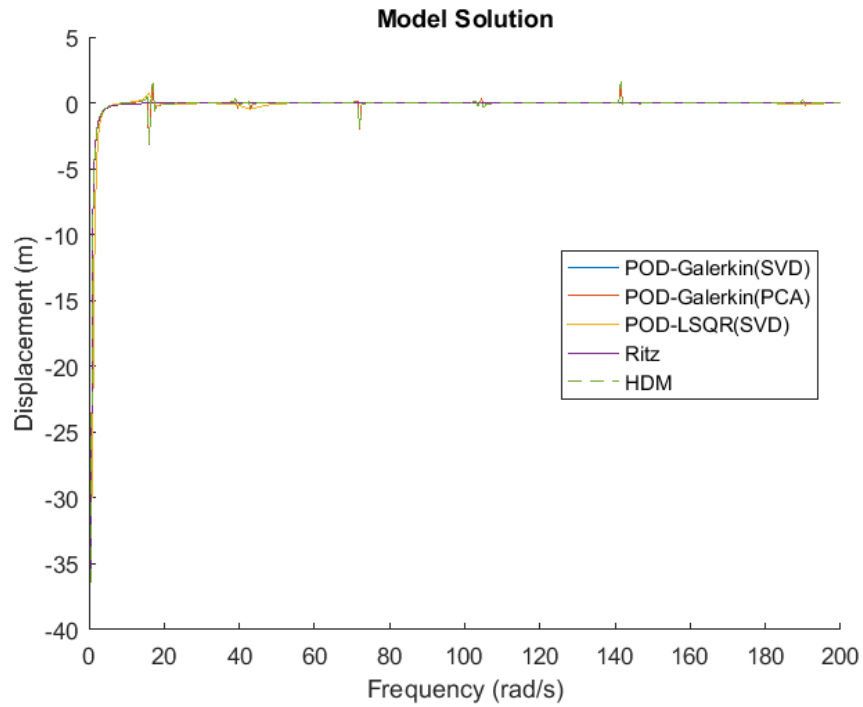

Figure 3.23: HDM and ROM solution corresponding to the force vector with 1000 N of magnitude.

Chapter 4

Structural Analysis and Reduction

4.1 Introduction

In this chapter, the reduction of a structural model with respect to a wing of a commercial aircraft will be explored. This option was made with the purpose of testing the MOR methods with a much higher number of degrees of freedom than the benchmark models, so that it can be shown that there can be a practical use of these methods in the aerospace industry. The main goal of this thesis is to study the computational time reduction achieved with model order reduction, consequently the structural design and stress analysis of the wing will not be fully explored. Nevertheless the geometric modulation and the results of the stress analysis resulting from a FEM analysis of the model will have characteristics and convergence checks so that it could be upgraded to a more realistic and detailed model.

To delve in the question of the reduction of the computational time of this model, a dynamic analysis will be performed using the dynamic equilibrium equations 2.15, which have been the core element of the reduction methods presented in this thesis. The MOR methods implemented in this chapter will be the POD-Galerkin (SVD variant) and the POD using the least mean square method. The FEM will be used to formulate the dynamic equilibrium equations, as it was done for the benchmarks models in the last chapter.

The chapter will begin with the formulation and analysis of the structural model in question and after that the MOR methods mentioned before will be applied to the model.

4.2 Structural Model Formulation and Simulation

4.2.1 Model Formulation

The wing structure that was chosen to be the target for the MOR studies of this thesis is inspired in the wing of th Boeing 777 commercial aircraft. It has to be emphasized that several components of the wing structure were simplified, for example, the ribs and spars are assumed as thin plates with no holes and no caps, the total number of ribs was reduced from 40 to 10 ribs, all the stringers were suppressed as

well as all the joints and fittings that should be connecting all these structural elements.

Another important assumption, which reduces significantly the complexity of this structure, is that only one material was considered for the whole model. In practice, each element of a wing can have a different material, because variables like the mechanical strength, ductility, fatigue resistance and processes of manufacture can influence the mechanical proprieties of the materials and consequently effecting the mechanical behaviour of the airframe elements.

In the subject of airframe materials, one can not forget to mention composite materials, which have been a trending topic in the last few decades. These materials require different analysis criteria, like the deformation and stress state in each ply, which result in the failure indices that are commonly used for composite structure analysis [47], thus implying a more exhaustive analysis too. Since this thesis focus only on the simulation time of the model these topics were here neglected, although they can be addressed in a future work. Therefore the material that was defined for the whole structure was the Aluminum alloy 2024-T4 [48], because it is the most common material encountered in airframe structures and may be used as a reference for many pre-design analysis [49].

The wing plan which was used for reference in the modulation of this structure is represented in figure 4.1 and the respective geometric modulation is illustrated in figure 4.2. The wing was modeled with no torsion, a wing span of 20 meters and the airfoil chosen is the supercritical airfoil NASA SC(2)-0714, which began to be used in commercial transport airplanes in the early 70's and it remains widely used in modern commercial aircrafts [50]. These aircrafts have a design cruise speed in the transonic regime, which implies that there will be a shock wave formation in the upper surface of the airfoil. A supercritical airfoil will produce a shock wave closer to the trailing edge, unlike the standard NACA 6-series airfoil, thus reducing drag and vibrations induced by the shock wave.[51]

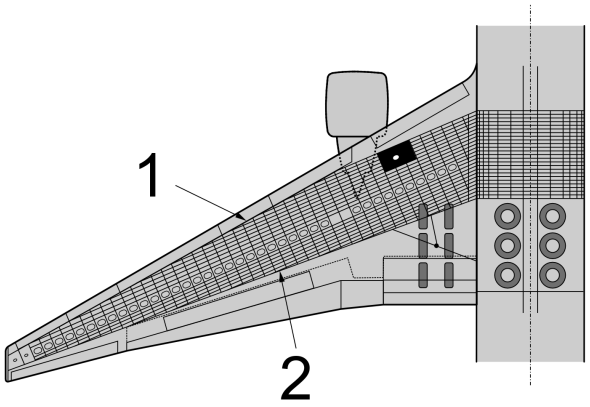

Figure 4.1: Boeing B-777 wing plan with the front and rear spar indicated with the number 1 and 2, respectively.[52]

The geometry design, domain discretization and solving of this model were carried out using Ansys.

Since the MOR methods will need the mass and stiffness matrices, along with the load vector, a modal analysis is also needed to obtain this data.

The cruise conditions of this wing's aircraft can be simulated by a CFD analysis, thus allowing for a better understanding of the behaviour of the structural model and consequently having a basic validation

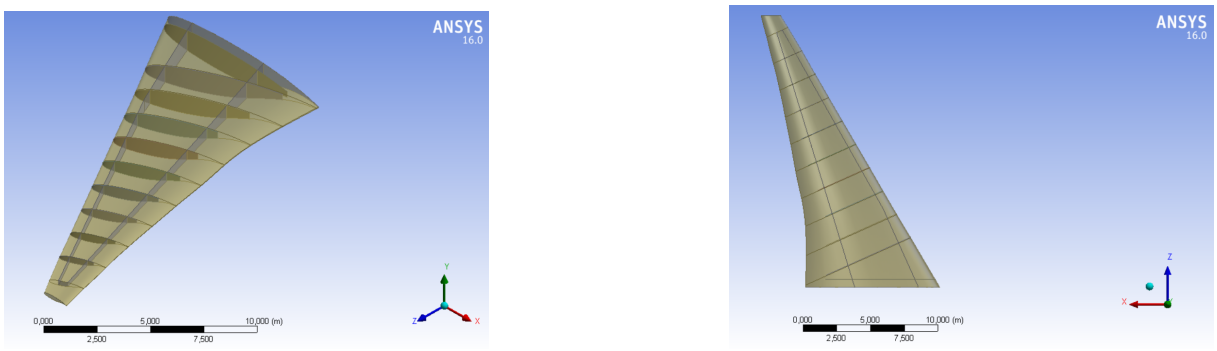

(a) Isometric View (b) Top View

Figure 4.2: Geometric design of the structural model.

of the respective model. Therefore to obtain a precise result of the pressure distribution caused by the aerodynamic load, a computational fluid dynamic (CFD) analysis of the wing is performed, also using the Ansys software. Therefore two kind of analyses will also be performed: a CFD analysis for the determination of the load/input vector; and a structural analysis using that input for the determination of the displacements of the structure. The coupling system module of Ansys will be responsible for the connection between these two analyses. Figure 4.3 represents the schematic of the analysis here described.

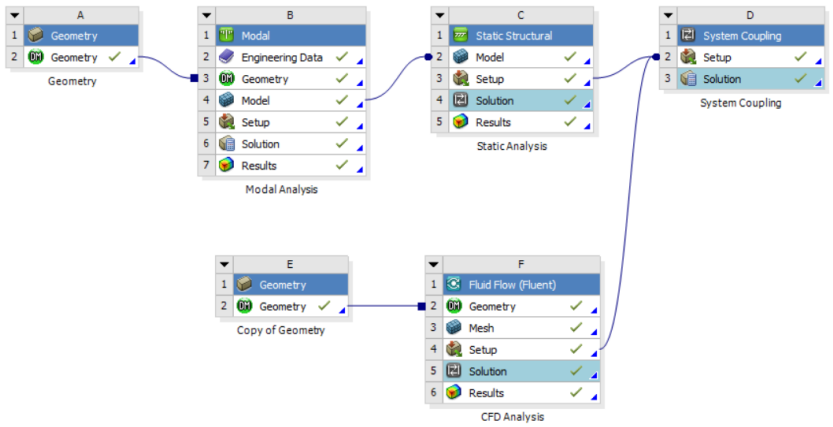

Figure 4.3: Ansys model scheme.

The boundary conditions for the structural model are the aerodynamic pressure distribution derived in the CFD model and applied on the skin panels of the wing structure. The constraints are defined at the root of the wing by restraining every degree of freedom of each node that is in the root plane of the wing.

In the case of the CFD model the domain's geometry consists in a half cylinder with one spherical base and a cavity, which is inserted in the middle of the domain, with the exterior shape of the wing. This is the domain that will be discretized with finite volume elements and can be seen in figure 4.4. The inlet boundary condition is defined in both the spherical base and the curved lateral face of this geometry. The inlet condition has a value of 251.39 m/s for the velocity magnitude and has an angle of attack of 3^{o}. The flat plane that cuts the cylinder in half has a symmetry boundary condition, its flat base is the

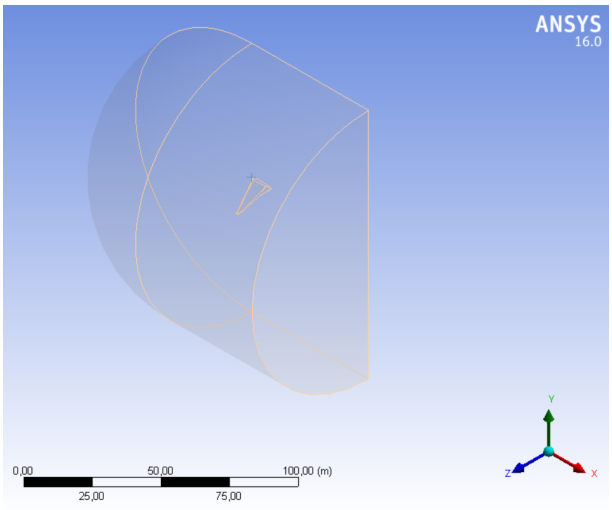

Figure 4.4: CFD fluid domain.

outlet condition at constant atmospheric pressure and the wall representing the exterior surface of the wing has a no slip condition.

The mesh of the structural model consists in Ansys *Quad4* and *Tri3* finite elements. The *Quad4* is a 2-D element with 6 degrees of freedom in each node, which models thin plate and membrane behaviour. The *Tri3* is used exceptionally in the mesh, since this element is a constant strain element, it needs to be avoided, specially in zones of high stress concentrations. This last element is also a 2-D element which models thin plate and membrane behaviour. Since no caps or fasteners were modeled, the mesh is connected by equivalencing the nodes near the interfaces between the ribs, spars and skin panel.

The CFD mesh uses 4 kinds of finite volume elements. The most used element is the tetrahedron element *Tet4*, which despite not being the most accurate element, can easily generate a mesh in most of CFD domains, so this was why this was the most used element in the outer part of the domain, where no critical flow zones are present. The second most used finite volume is the triangular prism which is a more accurate element to model the boundary layer pressure gradient, since its lateral faces can have high aspect ratios, which is a desirable propriety for the study of the boundary layer region of the flow. The mesh inflation zone is part of the fluid domain where high pressure gradients will be developed due to boundary layer conditions, thus this is where the triangular prism element will be applied and since this is a critical flow zone, the mesh has to be more refined. One of the most important parameters of a CFD mesh is the y+, which corresponds to the height of the inflation zone; this parameter will be discussed in section 4.2.2 of this thesis. The other used finite volumes were the hexahedron and the pyramid, these elements were used in 1% of the total mesh domain.

The values used for the air density and dynamic viscosity in the CFD simulation were 0.4135 kg/m^3 and 1.458e-5 kg/ms, respectively [53]. This values were relative to the cruise altitude of the Boeing 777, which is approximately 10000 meters above sea level [54]. Thus using the following mean chord formula for this tappered wing:

$$\bar{c} = \frac{2}{S}\int_0^{b/2} c(y)^2 dy, \tag{4.1}$$

where S is the area of the wing, b is the wing span and $c(y)$ is the wing chord at the coordinate y, which corresponds to a point in the span of the wing. The values used were $S = 217.01\text{m}^2$, $b = 38.4\text{m}$ and $c(y) = -0.426 \times y + 9.95$, resulting in $\bar{c} = 6.91\text{m}$. Now the Reynolds number of the CFD simulation can be derived by the following equation:

$$Re = \frac{\rho U \bar{c}}{\mu} = \frac{0.4135 \times 251.39 \times 6.91}{1.458e-5} = 4.927e7 \tag{4.2}$$

4.2.2 Convergence Analysis

In order to validate the case study model used in this chapter, a convergence analysis and result check will be performed in this section, thus the schematic represented in figure 4.3 is the one which is going to be used for this purpose. This schematic represents the three types of analysis used in this model:

- Modal Analysis- This analysis will be responsible for the derivation of the mass and stiffness matrices, which will define the structural model using the 2.15 equation. The constraints are also defined in this analysis.
- CFD Analysis- In this analysis the aerodynamic pressure distribution required as input for the static analysis will be computed.
- Static Analysis- This structural analysis will solve the model formulated by the modal analysis, using the input of the CFD model, thus providing as outputs the displacements and stresses of the structure.

The system coupling block is responsible for the connection between the pressure distribution output of the CFD analysis and the load input vector of the static structural analysis. It will basically translate the aerodynamic pressure distribution into a load vector necessary the solving the structural model.

Structural Model Convergence

Since the discretization of the domain and constraints of the model are defined in the modal analysis, the natural frequencies of the structure will be one of the outputs of this analysis and can serve as reference for the convergence of this model. In figure 4.5 are shown the plot of the first 6 natural frequencies of the wing structure in respect to the number of elements used in the domain's discretization. In table 4.1 the relative errors of the meshes used in the convergence analysis are shown. These errors were derived in relation to the most refined mesh, which has 41406 elements. It can be concluded from both figure 4.5 and table 4.1 that the model's natural frequencies converge to a constant value as the number of elements increases.

CFD Model Convergence

The reference outputs for the convergence study of the CFD model are the lift coefficient (C_L) and drag coefficient (C_D). The plots presented in figure 4.7 demonstrate the convergence of both these coefficients to a constant value with an increase of the element number used in the mesh.

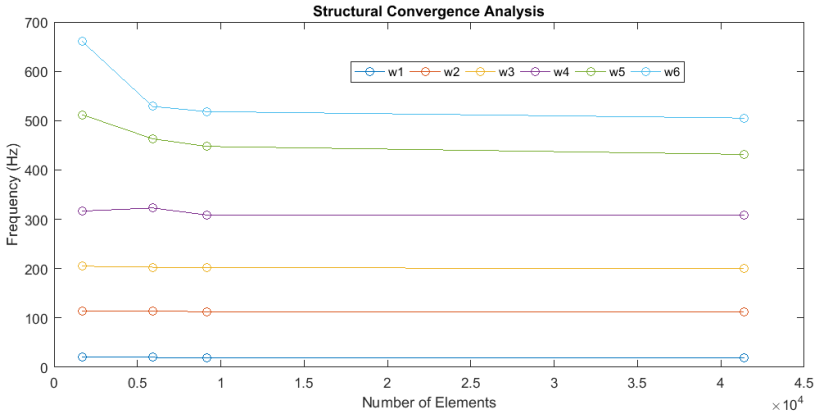

Figure 4.5: Structural model convergence plot.

	Number of Elements		
	1681	5908	9153
$e_{r_{w1}}(\%)$	1.520	1.104	0.122
$e_{r_{w2}}(\%)$	1.735	1.459	0.116
$e_{r_{w3}}(\%)$	2.210	1.202	0.599
$e_{r_{w4}}(\%)$	2.789	4.821	0.240
$e_{r_{w5}}(\%)$	18.633	7.319	3.721
$e_{r_{w6}}(\%)$	30.776	4.674	2.605

Table 4.1: Relative error of the meshes used in the structural convergence analysis, in respect to the most refined one.

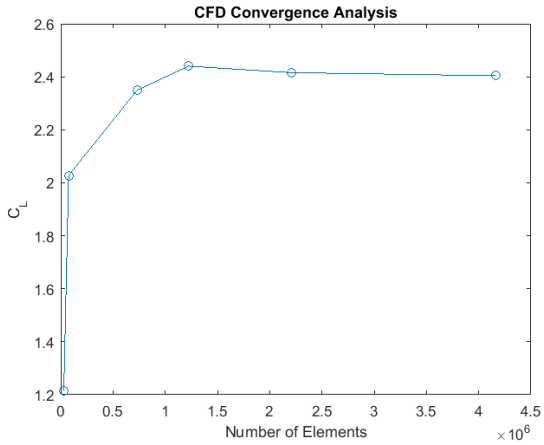

Figure 4.6: C_L convergence plot.

	Number of Elements				
	29410	75311	729326	1223155	2206993
$e_{C_L}(\%)$	49.449	15.658	2.275	1.506	0.487
$e_{C_D}(\%)$	109.361	107.221	14.143	11.273	4.378

Table 4.2: Relative error of the meshes used in the CFD convergence analysis, in respect to the most refined one.

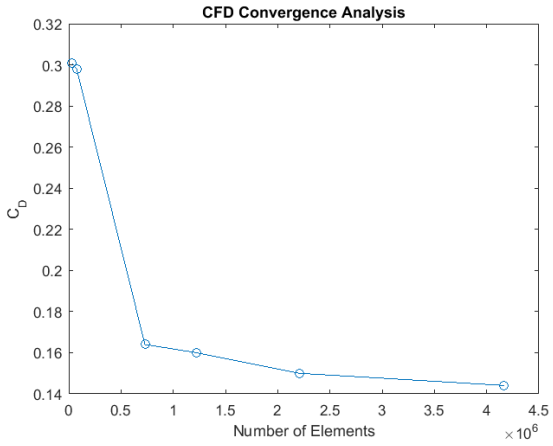

Figure 4.7: C_D convergence plot.

The discretization of the CFD simulation domain is more refined when closer to the wing wall, as it can be seen from figure 4.8. The inflation zone of the mesh was controlled by the parameter y+, which had a value of 5 millimeters, applied in 5 layers with a growth rate of 1.2. This was applied to all the simulations done for the convergence study. The value of the y+ should be considerably smaller for the simulation of a flow with a Reynolds number of this magnitude, but the choice of a smaller value would result in a excessive use of the RAM memory of the laptop used in this calculation, resulting in a crash of the CFD software. Since the y+ has more influence on the study of the boundary layer, consequently its refinement will have more impact on the calculation of the C_D and in the precision of the determination of the flow regime. The presence of the inflation zone in the mesh can bee seen in figure 4.8.

Having a more precise calculation of the transition of the flow regime has an impact on the determination of the pressure distribution, because the precise simulation of this flow characteristic defines the flow regime in the chordwise direction, which has a considerable impact on the C_L of the wing, specially when separation occurs, which would be odd to happen in a flow with an angle of attack of 3º.

In order to converge the solution of this model with the y+ value mentioned before and since the drag coefficient is not the major target of study in this thesis, the choice of the turbulence model considered may facilitate the convergence of the solution, thus the turbulence model chosen was the Spalart-Allmaras. This turbulence model is less sensitive to the y+ values, consequently facilitating the convergence of this solution, even though it introduces error in the C_D calculation.[55]

Results

With the convergence study of both the CFD and the structural models done successfully and despite the model's low fidelity assumptions, a check on the behaviour of the structure was made. The main goal of this check is to make sure that at least the maximum Von-Mises stress derived by the FEM, when multiplied by a safety factor of 1.5, would not be greater then the yielding stress of the material, thus guaranteeing that the model remains in the linear regime. The parameter which controlled the Von-Mises values was the thickness of the structural elements (spar, ribs and skin panels). These result checks were done using the structural mesh showed in the figures 4.9, 4.10 and 4.11 and the CFD mesh

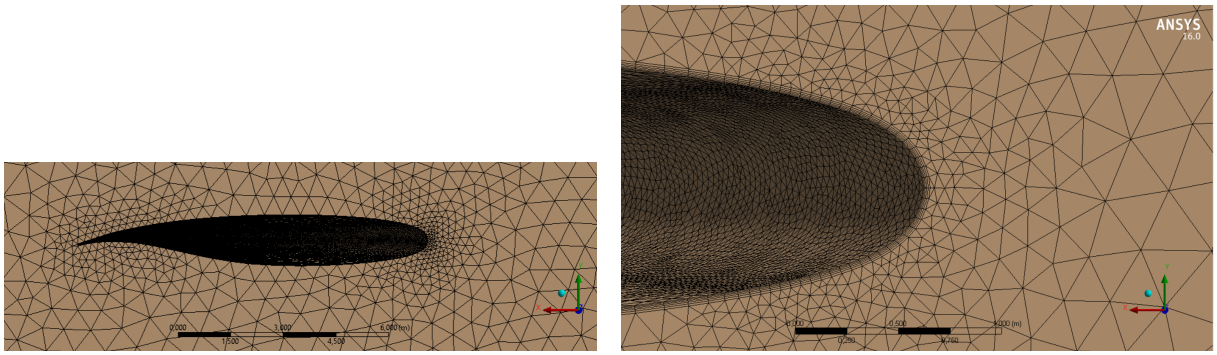

(a) CFD mesh on the root section of the wing.

(b) Inflation zone of the CFD mesh.

Figure 4.8: CFD Mesh.

represented in figure 4.12. These meshes correspond to the ones with more element numbers, which were used in the convergence analysis. It is known that there are more structural failure modes then just the ones considered here, but since the analysis in question targets only the linear static behaviour of this model, the material strength failure mode here considered can be seen as sufficient.

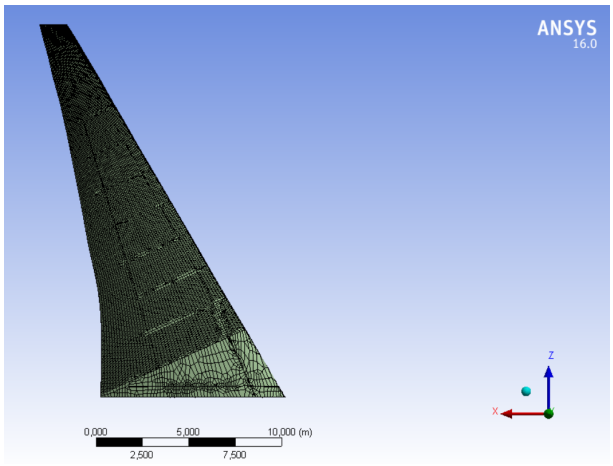

Figure 4.9: Mesh used in structural analysis results check. (Upper surface of the wing)

The final values of the thickness of each structural element are shown in table 4.4. These were the values used in the results present in table 4.3, which considering the roughness of the model, are acceptable, that is, the maximum equivalent stress value multiplied by the safety factor of 1.5 is not greater then the yielding stress of the material (Al 2024-T4) which corresponds to 324 MPa [48]. The displacements in respect to the y-axis direction and the equivalent Von-Mises stress plots are shown in figures 4.13 and 4.14, respectively. It can be seen in figure 4.15 that the maximum equivalent stress value occurs in one of the several stress concentration zones in the wing structure, namely in the connections between the rear spar and the ribs. These same zones arise due to the absence of fasteners, joints and fittings in the connections of the structural elements (that is why these zones are present in the connections between these elements). Despite the unrealistic values of the thickness defined for each structural element, these excessive values have to be considered as an assumption for this model, so that the discussion of this thesis does not delve in topics like material selection and structural opti-

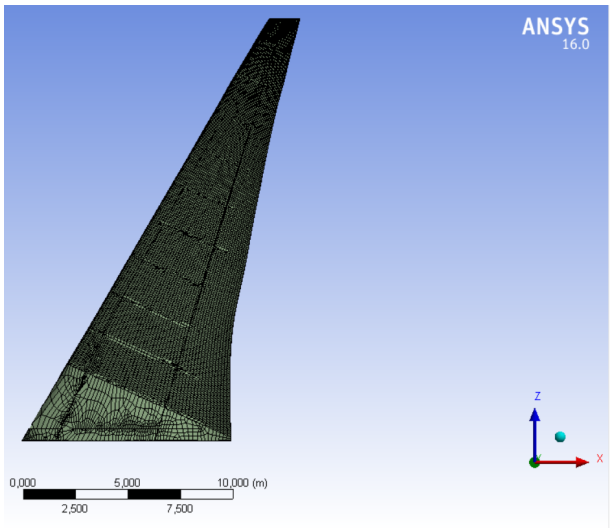

Figure 4.10: Mesh used in structural analysis results check. (Down surface of the wing)

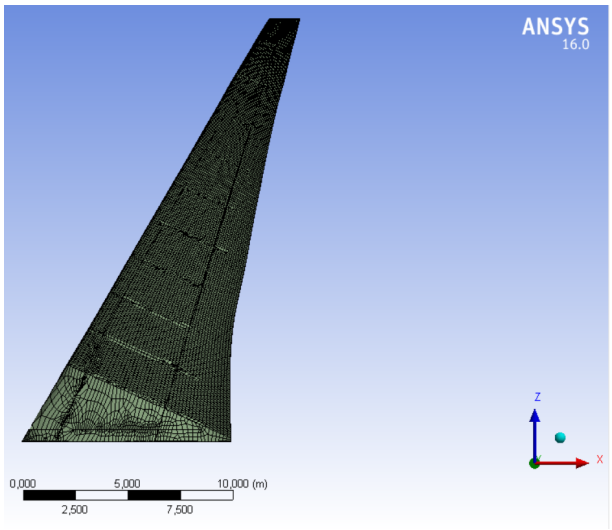

Figure 4.11: Mesh used in structural analysis results check. (Inside components of the wing)

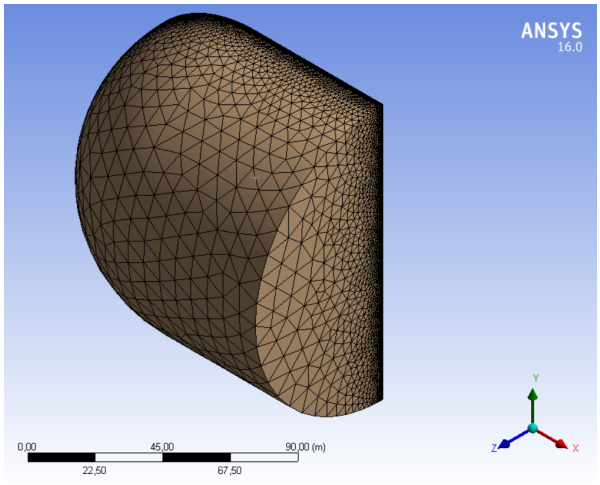

(a) Isometric view of CFD mesh.

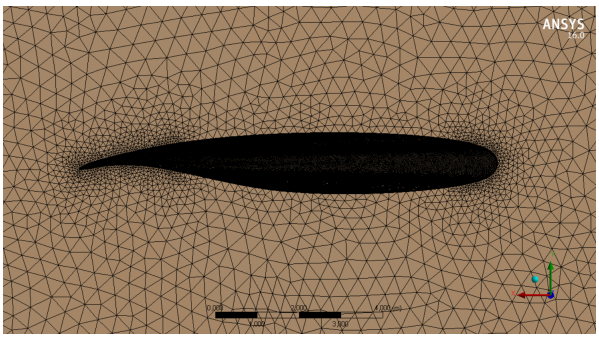

(b) Root Section of CFD mesh used in the results check.

Figure 4.12: Mesh used in CFD analysis results check.

mization. Therefore the check for a basic validation of this model can be obtained successfully with the results obtained by the analysis presented in this section.

The pressure distribution on several sections of the wing, which was obtained using the mesh plotted in figure 4.12 is shown from figure 4.16 to figure 4.18.

Max. Displacement in y-direction (m)	Max. Von-Mises Stress (MPa)
0.617	199.586

Table 4.3: Summary of structural analysis results.

Strtuctural Elements	Thickness (mm)
Skin	10.0
Spars	30.0
Ribs	10.0

Table 4.4: Thickness of structural elements used in the model.

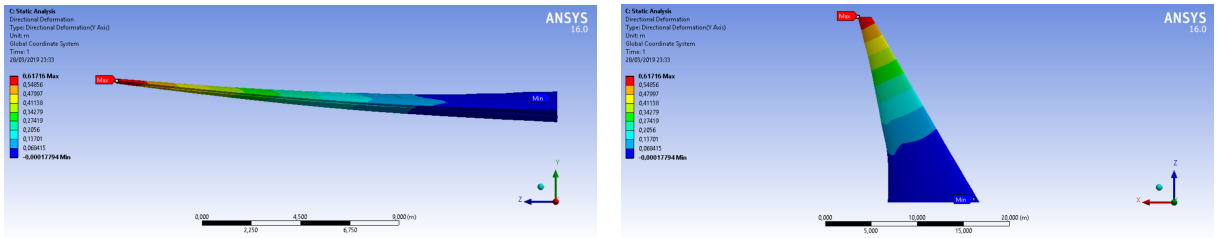

(a) Front view. (b) Top view.

Figure 4.13: Structural displacement plot.

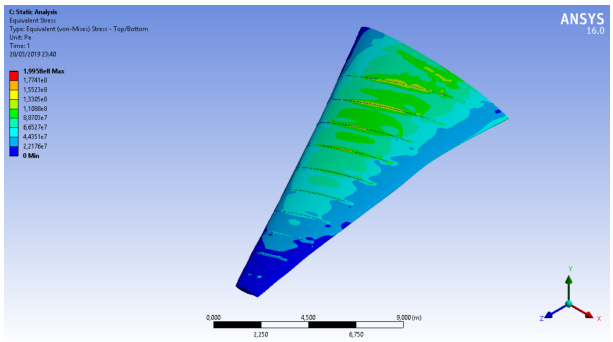

Figure 4.14: Equivalent Von-Mises stress plot.

4.3 Structural Model Reduction

4.3.1 Introduction

Since the structural model of the wing is already formulated, a dynamic analysis of the system can now be done and it will be the target of the MOR methods, as it was done for the benchmark examples. The

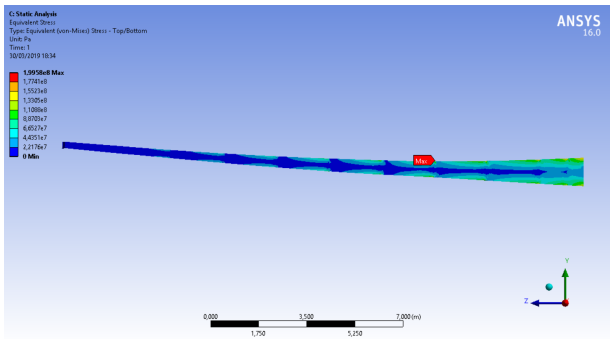

Figure 4.15: Stress concetration in rear spar.

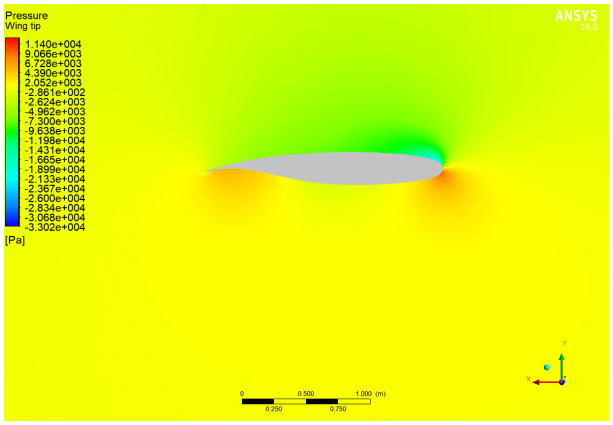

Figure 4.16: Pressure distribution on tip section of the wing. ($y = 19m$)

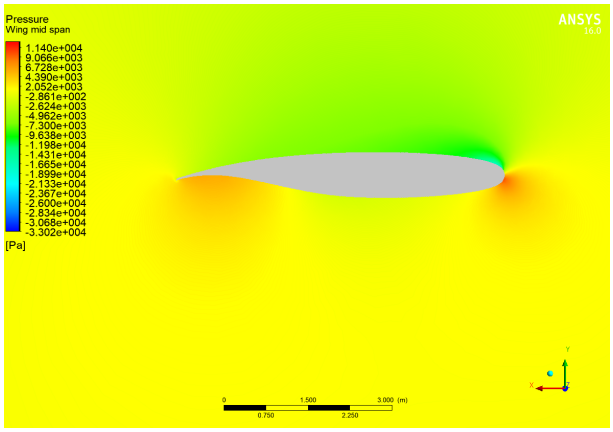

Figure 4.17: Pressure distribution on mid section of the wing. ($y = 8m$)

model has 223860 degrees of freedom and is represented by the dynamic equilibrium equations used in the benchmarks presented in sections 3.2 and 3.3. The dynamic equilibrium equation is represented by:

$$\mathbf{M}\ddot{\mathbf{x}} + \mathbf{K}\mathbf{x} = \mathbf{f}, \tag{4.3}$$

The mass matrix $\mathbf{M}$ and the stiffness matrix $\mathbf{K}$ are the ones used in the Ansys solver resulting from the domain discretization made in that software. The load vector $\mathbf{f}$ for this example is a result of an oscillatory force imposed at the nodes of the wing tip and two other oscillatory forces applied at the

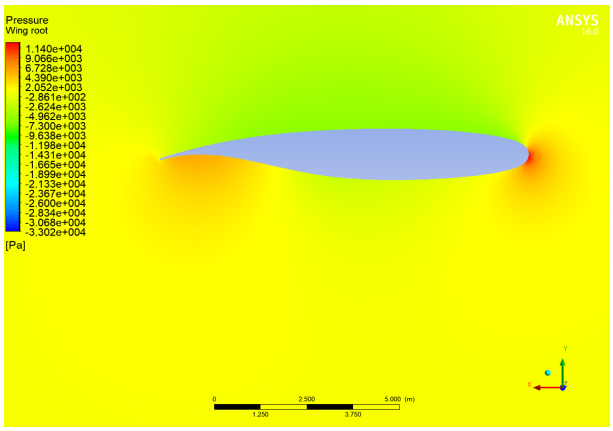

Figure 4.18: Pressure distribution on root section of the wing. ($y = 0m$)

nodes which connect the wing spars to its skin panels. The purpose of this last two forces is to mimic the torsion behaviour of the wing, that is why they have the same characteristic, but have an opposite direction in order to induce the binary necessary so that there can be a torsion motion of the structure. The three loads can be represented by the following equations:

$$f(t)_1 = 100000\text{sin}(0.314(\text{rad/s}) \times t) \quad (N), \tag{4.4}$$

$$f(t)_2 = 500000\text{sin}(0.314(\text{rad/s}) \times t) \quad (N), \tag{4.5}$$

$$f(t)_3 = -500000\text{sin}(0.314(\text{rad/s}) \times t) \quad (N), \tag{4.6}$$

where $f(t)_1$ is respective to the force applied at the wing tip and $f(t)_2$ and $f(t)_3$ are respective to the forces of the torsion binary imposed along the wing spars. All the three loads are applied in the y-axis direction.The magnitude of these forces was chosen such that the structural behaviour of the wing remains linear, thus the maximum Von-Mises stress derived by the Ansys solver and multiplied by a safety factor of 1.5 is below a tensile yielding stress of the material. The frequency chosen for this loads was determined so that an harmonic displacement as the one represented in figure 4.19 could be accomplished.

The dynamic analysis will be done in a time interval defined by $t \in [0; 10]$ s, with a time step of 0.2 seconds. The results obtained in the Matlab solver, which was used in the benchmark models, were verified by the results obtained using Ansys, thus allowing for the reduction of the model and its analysis using Matlab. The scheme used in this analysis is similar to the one showed on figure 4.3, the only change made was swapping the static analysis block to a dynamic analysis block. Figure 4.19 shows the vertical displacement (the displacement along the y-axis) of one of the degrees of freedom which is placed in the leading edge of the wing's tip. The time duration for solving the HDM with the Matlab solver is presented in table 4.5.

The MOR methods which are going to be explored is this section are:

- POD - Galerkin Projection (SVD variant). (POD - Galerkin)

HDM computation time (s)
253.939

Table 4.5: Necessary computation time for the HDM solution.

- POD - Least Mean Squares. (POD - LMSQ)

The implementation of other MOR methods, like the POD-PCA or the Ritz method, was attempted. Although their algorithms require the multiplication of large matrices, which are not sparsed, in order to obtain the reduced model, their implementation was not successful since the RAM memory required for these operations exceeded the available computer RAM memory (32 Gb). The methods which are going to be explored in this section were ran in the same computer as the models presented in chapter 3, using the Matlab software. The POD-LMSQ also uses the SVD as the basis method, like it was done for the benchmarks presented in chapter 3.

In the next sections of this thesis the results obtained by the MOR methods are compared with the HDM solution and the time reduction is also going to be analyzed.

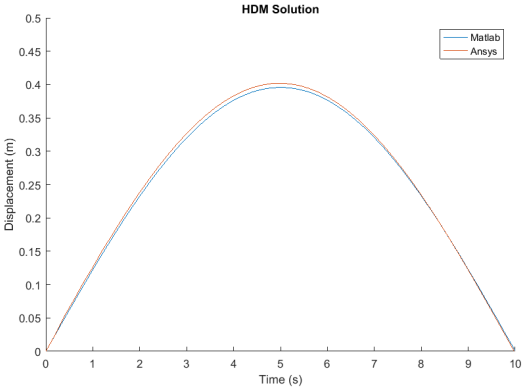

Figure 4.19: HDM solution - Vertical Displacement of a node placed in the leading edge of the wing tip.

4.3.2 Results and discussion

Error estimation and analysis

The POD-Galerkin method was implemented using three different values of snapshot spacing (ΔS). The projection errors associated with this method for the three ΔS values are presented from figure 4.20 to figure 4.22. In these plots the colinear, orthogonal and total errors are presented in relation to the ROM's order. The figures show that the projection error decreases as the ROM's order is increased, which proves that the ROM results converge in respect to their order for all three ΔS values. The main difference between the three ΔS values is that there is a decrease in the error when there is an decrease in the ΔS value. The total error for the sixth order ROM is presented in table 4.6, so that the error variation relative to the snapshot spacing is more explicit. The error behaviour for these three cases is similar and it shows that a considerably small value (less than 5%) is reached for a third and

higher ROM order.

	$\Delta S = 10$	$\Delta S = 5$	$\Delta S = 1$
e_{tot}	2.392e-4	1.951e-7	1.004e-7

Table 4.6: POD-Galerkin sixth order ROM projection error variation in relation to ΔS.

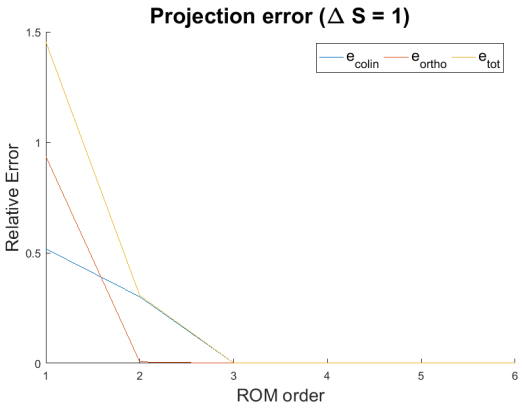

Figure 4.20: Projection error estimation for the POD-Galerkin for $\Delta S = 1$).

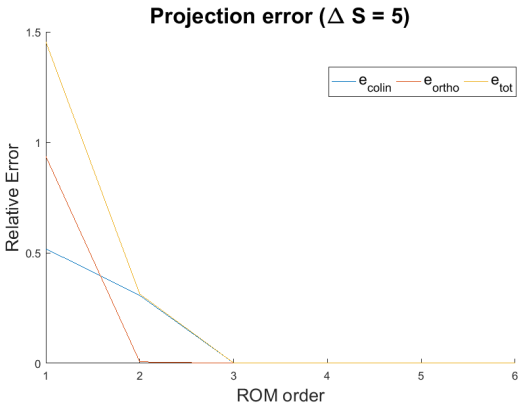

Figure 4.21: Projection error estimation for the POD-Galerkin for $\Delta S = 5$.

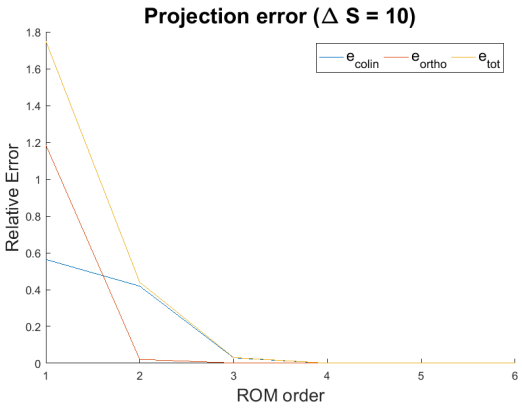

Figure 4.22: Projection error estimation for the POD-Galerkin for $\Delta S = 10$.

In the case of the POD-LMSQ there will not be any projection error, since the algorithm does not use the projection process to obtain the reduced space. Therefore the error analysis for this method will be based on the output error, which was also used in the benchmarks presented in chapter 3. Since the output error also applies to the POD-Galerkin, it will be used as a comparison reference between these two methods. Figures 4.23, 4.24 and 4.25 show the output error for both the POD-Galerkin and POD-LMSQ in relation to their ROM's order. It can be drawn from this figures that the output error remains practically the same for all the three ΔS cases and that the output error also stabilizes at the third order ROM. Table 4.7 show the values of the output error for the sixth order ROM and for all the three cases.

Both the ROM solutions of the degree of freedom depicted in figure 4.19 are presented in the plot of figure 4.26 along with the HDM solution. The reduced solutions come from a sixth order ROM for both cases. The plots depicted in figure 4.26 are hard to distinguish, since all the three solutions are practically similar.

Method	$\Delta S = 10$	$\Delta S = 5$	$\Delta S = 1$
POD-Galerkin	7.144e-8	5.006e-11	2.393e-11
POD-LMSQ	1.972e-5	2.160e-7	1.259e-8

Table 4.7: Sixth order ROM output error variation in relation to ΔS.

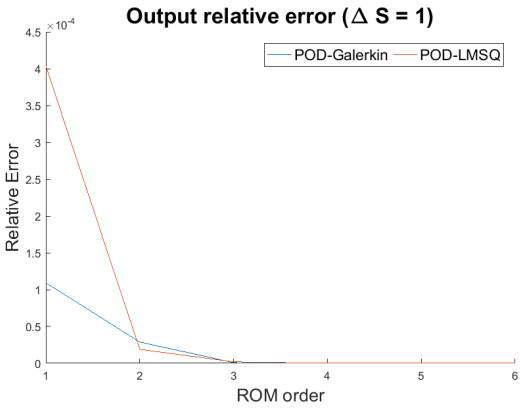

Figure 4.23: Output error estimation for both POD methods ($\Delta S = 1$).

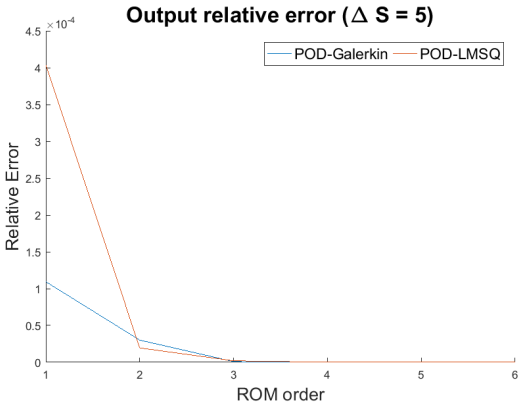

Figure 4.24: Output error estimation for both POD methods ($\Delta S = 5$).

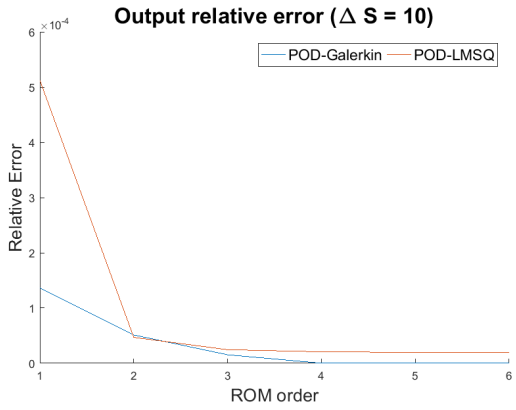

Figure 4.25: Output error estimation for both POD methods ($\Delta S = 10$).

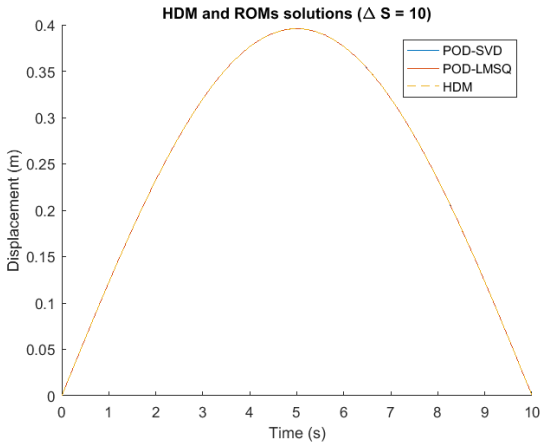

Figure 4.26: HDM and ROM solution plot - Vertical Displacement of a node placed in the leading edge of the wing tip.

Time duration analysis

The time performance of the POD-Galerkin and POD-LMSQ is presented in tables 4.8 and 4.9, respectively. As it was shown in the last chpater, the sample time will decrease with the increase of the ΔS value in both methods. Since the SVD is the common basis method for both methods, the basis time increases with the ΔS value in both cases. The main difference between the time performance of these methods is the solve time, which is smaller in the case of the POD-Galerkin method. For this reason the POD-Galerkin has a slightly best time performance. In both cases the solve time decreases with the increasing of the ΔS value.

ΔS	Sample time(s)	Basis time(s)	Reduction time(s)	Solve time (s)	Total time(s)	t_r (%)
1	0.238	0.991	0.098	6.611e-4	1.327	99.506
5	0.053	0.078	0.097	6.290e-4	0.229	99.915
10	0.025	0.036	0.105	2.650e-4	0.166	98.938

Table 4.8: Time analysis for the sixth order ROM obtained via POD-Galerkin.

ΔS	Sample time(s)	Basis time(s)	Reduction time(s)	Solve time (s)	Total time(s)	t_r (%)
1	0.245	1.007	0.090	1.422	2.762	98.972
5	0.046	0.075	0.089	2.367	2.577	99.041
10	0.024 0.037	0.093	2.876	3.031	98.872	

Table 4.9: Time analysis for the sixth order ROM obtained via POD-LMSQ.

Chapter 5

Conclusions

It was shown in this thesis that there can be a reduction on structural analysis computational time, through MOR methods, with a conservation of the solution's quality. The background research done on chapter 2 consisted in presenting the state-of-the-art related to the MOR techniques which apply to the computational study of structural systems formulated by ODE models. From this research it was drawn that there can be four types of MOR methods applied to structural mechanics:

- Physical coordinate methods.
- Projection based generalized coordinates methods.
- Other generalized coordinates methods.
- Hybrid coordinates.

The main physical coordinates method is the Condensation method, which uses the same physical coordinates for the HDM and ROM solutions. In the case of the projection based generalized coordinates methods the HDM is projected in a reduced space. This projection is made with a coordinate transformation matrix which is denominated by the reduction basis. The reduction basis is derived based on a sample of the HDM's solution. In the case of the generalized coordinates methods using the least mean square algorithm, the reduction basis is still needed, but in this method a minimization of the residue of the original equations in the reduced space is done. The hybrid coordinates uses both physical and generalized coordinates, for example, using the static condensation which would be applied to the slave degrees of freedom and then a reduction in the modal space is applied to the master degrees of freedom [38].

In order to test the methods presented in chapter 2, several benchmark models were reduced. The formulation and solution of this models was already done in previous works. In this benchmarks the error estimation and time performance of the MOR methods were verified. This study allowed for a better understanding of the behaviour of each MOR technique.

After the benchmark reductions, a finite element model of a simplified wing structure was made, so that it could be verified that the MOR techniques here presented could be applied to an actual airframe

structure. Many assumptions were made in this model, for example, considering that the structure was all composed from the same material, which resulted in exaggerated thickness of its structural components. Another assumption was considering just three structural components: ribs, spars and skin panels. In order to validate this simplified model a CFD analysis simulating the cruising conditions of this wing's aircraft was done. It was verified that the wing had an acceptable deflection and that the Von-Mises stress felt by the components of the structure was not higher than the material's ultimate stress. Lastly, the MOR methods were tested using the already mentioned airframe structure.

5.1 Achievements

The MOR methods applied successfully in the benchmark models were both the POD-Galerkin variants (SVD and PCA), POD-LMSQ, the static Ritz vector method and the mode displacement method. Only the condensation method struggled in this implementation phase. All the other reduction methods had their error estimations below 5% and a time reduction approximately equal to 99% relative to the HDM computation time. The same was verified in the wing structure model for which the POD-Galerkin (SVD variant) and the POD-LMSQ were applied, proving that these methods can be easily applied in the computational analysis of airframe structures. The other methods which were successfully applied in the benchmark models required an excessive amount of RAM memory, which make them unfeasible solutions for the wing structure model that present much more degrees of freedom.

5.2 Future Work

With the research made in this thesis, one can conclude that there are many topics which should be using MOR in the study field of computational mechanics, more specifically in structural analysis. These topics can be: structural optimization using MOR methods [56]; ROM interpolation[3–6]; the study of other methods which have not be fully explored like the PGD [35–37] or MOR techiques using AI [7, 8] or even hybrid coordinates methods [38, 39] can also be a target for future work. Lastly the airframe structure model here presented can be uploaded in the MOR benchmark database used in this thesis [40], so that it could contribute to the research in this area of study.

Bibliography

[1] F. Afonso, J.Vale, F.Lau, and A.Suleman. Performance based multidisciplinary design optimization of morphing aircraft. *Aerospace Science and Technology*, 67:1–12, 2017.

[2] G. da Cunha Laboreiro Mendonça. Model order reduction for aerodynamic lifting surfaces. Master's thesis, Instituto Superior Técnico - Universidade de Lisboa, 2017.

[3] A. J. Keane and P. B. Nair. *Computational Approaches for Aerospace Design*. John Wiley and Sons, Ltd, 2005.

[4] S. A. Renganathan, Y. Liu, and D. N. Mavris. A methodology for projection-based model reduction with black-box high-fidelity models. *Engineering Structures*, 2017.

[5] D. Amsallem, J. Cortial, K. Carlberg, and C. Farhat. A method for interpolating on manifolds structural dynamics reduced-order models. *International Journal for Numerical Methods in Engineering*, 80:1241–1258, 2009.

[6] D. Amsallem and C. Farhat. An online method for interpolating linear parametric reduced-order models. *SIAM Journal on Scientific Computing*, 33:2169–2198, 2011.

[7] H. Salehi and R. Burgueño. Emerging artificial intelligence methods in structural engineering. *Engineering Structures*, 2171:170–189, 2018.

[8] A. Oishi and G. Yagawa. Computer methods in applied mechanics and engineering. *Engineering Structures*, 327:327–351, 2017.

[9] J. García-Martinez, F. Herrada, L. Hermanns, A. Fraile, and F. Montáns. Accelerating parametric studies in computational dynamics: Selective modal re-orthogonalization versus model order reduction methods. *Advances in Engineering Software*, 108:24–36, 2017.

[10] C. Farhat and D. Amsallem. Cme 345: Model reduction - projection-based model order reduction. Stanford University Model Reduction Coursework.

[11] I. S. and C. D. Model order reduction of nonlinear euler-bernoulli beam. *Nonlinear Dynamics - Conference Proceedings of the Society for Experimental Mechanics Series*, 1, 2016.

[12] G. Hallen and S. Ponsioen. Exact model reduction by a slow–fast decomposition of nonlinear mechanical systems. *Nonlinear Dynamics*, 90:617–647, 2017.

[13] G. Hallen and S. Ponsioen. Nonlinear model order reduction based on local reduced-order bases. *Numerical Methods in Engineering*, 92:891–916, 2012.

[14] R. Guyan. Reduction of stiffness and mass matrices. *AIAA Journal*, 30(3):891–916, 1965.

[15] Z.-Q. Qu. *Model Order Reduction Techniques*, chapter 4.1.2. 2004.

[16] U. Sellgren. *COMPONENT MODE SYNTHESIS - A method for efficient dynamic simulation of complex technical systems*. KTH-MMK, 2003.

[17] R. Henshell and J. Ong. Automatic masters for eigenvalue economization. *Earthquake Engineering and Structural Dynamics*, 3:375–383, 1975.

[18] Z.-Q. Qu. *Model Order Reduction Techniques*. 2004.

[19] F. Chinesta, R. Keunings, and A. Leygue. *The Proper Generalized Decomposition for Advanced Numerical Simulations*, chapter 1.2. 2014.

[20] B. Besselink and et al. A comparison of model reduction techniques from structural dynamics, numerical methods and systems and control. *Journal of Sound and Vibration*, 332:4403–4422, 2013.

[21] J. Gu, Z.-D. Ma, and G. M. Hulbert. A new load-dependent ritz vector method for structural dynamics analyses: quasi-static ritz vectors. *Finite Elements in Analysis and Design*, 36:261–278, 2000.

[22] E. L. Wilson, M. Yuan, and J. M. Dickens. Dynamic analysis by direct superposition of ritz vectors. *Earthquake Engineering and Structural Dynamics*, 10:813–821, 1982.

[23] D. D. Klerk, D. J. Rixen, and S. N. Voormeeren. General framework for dynamic substructuring: History, review and classification of techniques. *AIAA Journal*, 46:1169–1181, 2008.

[24] R. C. Jr. Coupling of substructures for dynamic analyses - an overview. *41ST STRUCTURES, STRUCTURAL DYNAMICS, AND MATERIALS CONFERENCE AND EXHIBIT*, 2000.

[25] W. A. Benfield, C. S. Bodley, and Morosow. Modal synthesis methods. *Space Shuttle Dynamics and Aeroelasticity Working Group Symposium on Substructures Testing and Synthesis*, 1972.

[26] S. Ullmann, M. Rotkvic, and J. Lang. Pod-galerkin reduced-order modeling with adaptive finite element snapshots. *Journal of Computational Physics*, 325:244–258, 2016.

[27] S. Ilbeigi and D. Chelidze. Persistent model order reduction for complex dynamical systems using smooth orthogonal decomposition. *Mechanical Systems and Signal Processing*, 96:125–138, 2017.

[28] Y.C.LIANG, H.P.LEE, S.P.LIM, W.Z.LIN, K.H.LEE, and C.G.WU. Proper orthogonal decomposition and its applications—part i: Theory. *Journal of Sound and Vibration*, 252:527–544, 2014.

[29] G. Kerschen, J.-C. Golinval, A. F. Vakakis, and L. A. Bergman. The method of proper orthogonal decomposition for dynamical characterization and order reduction of mechanical systems: An overview. *Nonlinear Dynamics*, 41:147–169, 2005.

[30] V. Lenaerts, G. Kerschen, and J. Golinval. Identification of a continuous structure with a geometrical non-linearity. *Journal of Sound and Vibration*, 262:907–919, 2003.

[31] T. Bui-Thanh, K. Willcox, O. Ghatas, and B. Waanders. Goal-oriented, model-constrained optimization for reduction of large scale systems. *Journal of Computational Physics*, 224:2:880–896, 2007.

[32] M. B. J. Weller and E. Lombardi. Numerical methods for low-order modeling of fluid flows based on pod. *International Journal for Numerical Methods in Fluids*, 63(2):249–268, 2010.

[33] C. W. Rowley, T. Colonius, and R. M. Murray. Model reduction for compressible flows using pod and galerkin projection. *Pysica D*, 189(1-2):115–129, 2004.

[34] C. C. Paige and M. A. Saunders. Lsqr: An algorithm for sparse linear equations and sparse least squares. *ACM Transaction on Mathematical Software*, 8:43–71, 1982.

[35] F. Chinesta, R. Keunings, and A. Leygue. *The Proper Generalized Decomposition for Advanced Numerical Simulations*. Springer, 2014.

[36] J. V. Aguado. *Advanced strategies for the separated formulation of problems in the Proper Generalized Decomposition framework*. PhD thesis, Université de Nantes - Faculté des Sciences et des Techniques, 2015.

[37] A. A. Takash, M. Beringhier, M. Hammoud, and J. C. Grandidier. On the validation of the proper generalized decomposition method with finite element method: 3d heat problem under cyclic loading. *Mechanism, Machine, Robotics and Mechatronics Sciences*, 58:3–13, 2019.

[38] J.-G. Kim, Y.-J. Parka, G. H. Lee, and D.-N. Kim. Improved hybrid dynamic condensation for eigenproblems. *37th Structure, Structural Dynamics and Materials Conference, Structures, Structural Dynamics, and Materials and Co-located Conferences*, 1993.

[39] A. Radermacher and S. Reese. Model reduction in elastoplasticity : Proper orthogonal decomposition combines with adaptive sub-structuring. *Computational Mechanics*, 54:677–687, 2014.

[40] The MORwiki Community. Mor benchmarks. MORwiki – Model Order Reduction Wiki, 2019. URL `http://modelreduction.org/index.php`.

[41] D. Billger. The butterfly gyro. In *Dimension Reduction of Large-Scale Systems*, volume 45 of *Lecture Notes in Computational Science and Engineering*, pages 349–352. Springer-Verlag, Berlin/Heidelberg, Germany, 2005. doi: 10.1007/3-540-27909-1_18.

[42] P. Pinsky and N. Abboud. Finite element solution of the transient exterior structural acoustics problem based on the use of radially asymptotic boundary conditions. *Computer Methods in Applied Mechanics and Engineering*, 85:311–348, 1991.

[43] K. Meerbergen. Fast frequency response computation for Rayleigh damping. *International Journal for Numerical Methods in Engineering*, 73(1):96–106, 2007.

[44] R. M. Ellis, P. C. Gross, J. B. Yates, and J. R. Casement. F-35 structural design, development, and verification. In *Dimension Reduction of Large-Scale Systems*, Aviation Technology, Integration, and Operations Conference. AIAA, 2018. doi: 10.2514/6.2018-3515.

[45] H. P. Gavin. Numerical integration in structural dynamics. 2016.

[46] O. B. Collection. Windscreen. hosted at MORwiki – Model Order Reduction Wiki, 2007. URL `http://modelreduction.org/index.php/Windscreen`.

[47] M. C. Y. Niu. *Composite Airfram Strtuctures*. Conmilit Press Ltd., 1997.

[48] M. Bauccio. *ASM Metals Reference Book*. Materials Park, 1993.

[49] T. C. Corke. *Design of Aircraft*. Prentice Hall, 2003.

[50] B. Gunston. Airbus, the complete story, 2009.

[51] C. Harris. Nasa supercritical airfoils: A matrix of family-related airfoils. Technical report, NASA, 1990.

[52] A. Sonorama. Aviation practice handbook, 2005.

[53] *Manual of the ICAO Standard Atmosphere*. ICAO, May 1954.

[54] *Type Certificate Data Sheet No.T00001SE*. FAA, August 2016.

[55] P. Spalart. Strategies for turbulence modelling and simulations. *International Journal of Heat and Fluid Flow*, 21:252–263, 2000.

[56] M. Zahr, Y. Choi, and C. Farhat. Design optimization using hyper-reduced-order models. *Structural and Multidisciplinary Optimization*, 51:919–940, 2015.